Selective localization of nanoparticles in microstructured systems

Giuseppe Nasti

Tutor:
Dr. Veronica Ambrogi

Co-tutors:
Dr. Gennaro Gentile
Dr. Pierfrancesco Cerruti

This dissertation is submitted for the degree of
Doctor of Philosophy
in
Materials and Structures Engineering
XXVIII cycle

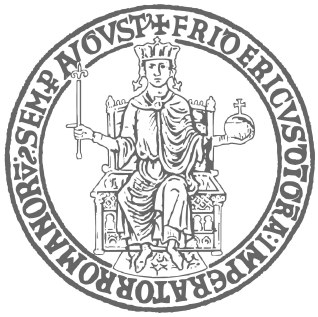

University of Naples "Federico II"
Department of Chemical, Materials and Production Engineering
Italy, March 2016

Contents

List of Figures

Acknowledgements

I would like to thank every single person that played a key role in the achievement of this milestone in my career. At the end of these three years a large number of people are worth of my gratitude for the amount of suggestions, constructive criticisms and encouragements received, although responsibility for any mistakes or inaccuracies in this text is mine alone.

My first thoughts go to my tutor, Dr. *Veronica Ambrogi*, and my two co-tutors Dr. *Gennaro Gentile* and Dr. *Pierfrancesco Cerruti*. Without them, none of this would have been possible. Although this expression often has formal tones I could not feel it more deeply. In this long journey they have been a continuous and endless source of scientific discussions, technical expertise, but especially of personal support and encouragement. They all know how much I needed their support.

I would like to thank the entire research team of Dr. *Pietro Ferraro*, and in particular Dr. *Sara Coppola*, for the competence, passion and energy they shared with me during the constructive and prolific scientific collaboration.

Similarly I want to thank the *Soft Matter Physics* group of Prof. *Ullrich Steiner* for the amazing experience I had in Switzerland. In particular, I cannot fail to mention Dr. *Antonio Abate*, the proponent of this collaboration, an exquisite person and a top-notch researcher that will be of inspiration inspiration for my future career.

I want to thank my closest and most loyal friends *Peppe*, *Rachele* and *Valentina*. Companions in work, travels, adventures, misadventures and *challenges*. You supported me, inspired me but above all you did bear me! Whatever the future will be I will never forget you.

Although an exhaustive list of persons who deserve a mention is not possible, I cannot fail to mention a few. My dear *Valeria*, affectionate counsellor. *Marta*, crazy friend. *Stella*, distant and adored. All the friends from IPCB, that I will not list because the risk of forgetting someone important would be to high. The ones who are part of it are aware.

And finally, because the last position in the acknowledgements is always the most prestigious, I thank my *family*. My *mother*, who tried to make

me strong. My *father*, who tried to make me righteous. My *sisters*, who showed me many aspects of the beauty of the world. Thank also to their *husbands* (actual and future one). I declare all my love to my (actual) *niece* and (future) *nephew*. You are the only constant of my life.

Ringraziamenti

Desidero ringraziare tutti coloro che hanno rivestito un ruolo fondamentale nel raggiungimento di questo nuovo traguardo della mia carriera. La quantità di suggerimenti, critiche costruttive ed incoraggiamenti ricevuti in tre anni ha portato a raggiungere un numero elevato di persone a cui la mia gratitudine è dovuta, sebbene a me soltanto sono imputabili eventuali errori e imprecisioni presenti nel testo.

Il mio primo pensiero va alla mia relatrice, la Prof.ssa *Veronica Ambrogi*, e ai miei due correlatori il Dott. *Gennaro Gentile* e il Dott. *Pierfrancesco Cerruti*. Senza di loro nulla di ciò sarebbe stato possibile. Sebbene tale espressione assuma spesso toni meramente rituali non potrebbe essere da me maggiormente sentita. In questo lungo percorso sono stati fonte continua ed inesauribile di conoscenze e consulenze tecniche, di discussioni e confronti scientifici, ma soprattutto di supporto e incoraggiamento personale. Ben sanno loro quanto abbia avuto necessità del loro sostegno.

Proseguo col ringraziare l'intero gruppo di ricerca del Dr. *Pietro Ferraro*, e in particolare la Dott.ssa *Sara Coppola*, per la competenza, la passione e l'energia che hanno messo a mia disposizione durante la formativa e prolifica attività di ricerca svolta in collaborazione con loro.

Similmente ringrazio il gruppo di *Soft Matter Physics* del Prof. *Ullrich Steiner* per la magnifica esperienza svolta presso il loro istituto in Svizzera. Non posso però non menzionare in particolare il Dott. *Antonio Abate*, fautore di questa collaborazione, persona squisita e ricercatore di prim'ordine a cui cercherò di ispirarmi nel prosieguo della mia carriera.

Voglio quindi ringraziare i miei più vicini e assidui compagni di viaggio *Peppe*, *Rachele* e *Valentina*. Compagni di lavoro, di viaggi, di avventure, di sventure e di *sfide*. Mi avete sostenuto, incitato ma soprattutto sopportato! Qualunque cosa accada in futuro, non potrò mai dimenticarvi.

Sebbene un elenco esaustivo delle persone che meriterebbero una menzione non sia possibile, non posso esimermi dal citarne alcuni. La mia cara *Valeria*, consigliera affettuosa. *Marta*, folle amica. *Stella*, lontana e adorata. Gli amici tutti dell'IPCB, una cui lista sarebbe tanto lunga da rendere il ris-

chio di dimenticare qualcuno di importante troppo elevato, per cui la eviterò. Chi vi appartiene, sa di farne parte.

E infine, perché l'ultima posizione nei ringraziamenti è da sempre la più prestigiosa, ringrazio la mia *famiglia*. Mia *madre*, che ha cercato di rendermi forte. Mio *padre*, che ha cercato di rendermi giusto. Le mie *sorelle*, che mi hanno mostrato diversi lati della bellezza del mondo. Ringrazio i loro *mariti* (attuale e futuro). Dichiaro tutto il mio amore ai miei *nipotini* (attuali e futuri tali). Siete l'unica costante della mia vita.

Abstract

The research activities carried out during the doctoral program focused on selective localization of nanoparticles in microstructured polymer systems. Three distinct processes, very different from each other, were employed to achieve similar results.

The first and main area of research, conducted at the Institute for Polymers, Composites and Biomaterials (IPCB-CNR, Pozzuoli), has involved the selective localization of the carbon nanotubes within a biphasic and bicontinuous blend of polystyrene and polylactic acid, obtained by melt mixing the two thermoplastic polymers. Nanoparticles were selectively dispersed in the polystyrene phase achieving a lower percolation threshold than the initial one.

In the second line of research, carried out in collaboration with the Soft Matter Physics group of the Adolphe Merkle Institute (Fribourg, Switzerland), hybrid organometallic perovkite nanocrystals were produced by precipitation in liquid phase. These nanocrystals were then incorporated into a thin film of polyethylene glycol diacrylate deposited by spin-coating on a glass substrate. The polymer crosslinking, triggered by exposure to an oxygen plasma, induced the formation of corrugations on the film surface (wrinkles) allowing the microstructuring of the perovskite.

In the third line of research, carried out in collaboration with the National Institute of Optics (INO-CNR), selective localization of quantum dots in polydimethylsiloxane microlenses on a pyroelectric lithium niobate substrate were achieved through electrohydrodynamic and dielectrophoretic mechanisms. The lithium niobate substrate was periodically poled in an hexagonal pattern using finite element simulations to predict the final position of particles.

Sommario

Durante il programma di dottorato sono state svolte tre diverse attività di ricerca riguardanti la localizzazione selettiva di nanoparticelle in sistemi polimerici microstrutturati.

La prima linea di ricerca ha riguardato la localizzazione selettiva di nanotubi di carbonio all'interno di una miscela polimerica bifasica e bicontinua, ottenuta tramite miscelazione a caldo, di polistirene e acido polilattico. Le nanoparicelle sono state disperse selettivamente nella fase polistirenica al fine di ottenere una soglia di percolazione elettrica inferiore rispetto a quella del sistema di partenza nanotubi/polistirene.

La seconda linea di ricerca è stata svolta in collaborazione con il gruppo di Fisica della Materia Soffice dell'Istituto Adolphe Merkle (Friburgo, Svizzera). In questo lavoro sono stati ottenuti nanocristalli di perovskite ibrida metallorganica tramite precipitazione in fase liquida. La dispersione di questi cristalli in una soluzione di polietilenglicole-diacrilato e toluene è stata usata per depositare un film sottile su di un substrato in vetro. La reticolazione e la microstrutturazione del polimero, e dunque dei nanocristalli in esso contenuti, sono state simultaneamente indotte dall'esposizione del substrato ad un plasma ad ossigeno.

Nella terza ed ultima linea di ricerca, svolta in collaborazione con l'Istituo Nazionale di Ottica (INO-CNR), è stata ottenuta la localizzazione selettiva di nanocristalli (quantum dots) in microlenti di polidimetilsilossano. Tale risultato è stato raggiunto sfruttando le forze elettroidrodinamiche e dielettroforetiche indotte da un campo piroelettrico. Tale campo elettrico è stato generato da un substrato di niobato di litio periodicamente polarizzato con domini esagonali. Simulazioni agli elementi finiti sono state effettuate al fine di determinare, computazionalmente, l'effetto del campo elettrico sulle particelle.

Chapter 1

Introduction

Nanoparticles and nanocomposites

Polymer composites have been used extensively for years in the fields of electrical insulation, vibrations damping and as high performance materials in automotive and aerospace. In all those fields used fillers were usually in the form of powders (micro-metrical sized) or as fibres, both dispersed or impregnated with thermosetting resins or melt mixed with thermoplastic polymers. The production of these composites requires the adoption of technologies that guarantee a good homogeneity of the materials, avoiding strong localised macroscopic variations of properties. Those localised heterogeneous part of the material can cause failures, breakages or the loss of functionality of the entire system. [1]

In recent years the introduction of a large variety of nano-metrical sized particles has opened many windows of opportunities in the composite field. A *nanoparticles* (NP) is defined as any material having at least one of the three dimensions below 100 nm. When NPs are added to a polymer matrix the system is defined *polymer nanocomposite* (NC). Three typology of NPs can be defined, depending on the number of particles dimensions below 100 nm: plate-like (one dimension, Figure 1.1a), fibrous (two dimensions, Figure 1.1b) and spherical (three dimensions, Figure 1.1c). All NPs have in common an exceptionally large surface area to volume ratio that maximize the interaction between the filler and the matrix. This interaction leads to a very efficient transfer of the particles properties to the final material. In Figure 1.1d the

Table 1.1: Surface area, volume and surface area to volume ratios of disks, cylinders and spheres.

Particles	**Volume** (A)	**Area** (V)	A/V
Disks	$\frac{\pi}{4}d^2 s$	$\pi d(\frac{d}{2}+s)$	$\frac{2}{s}+\frac{4}{d}$
Cylinders	$\frac{\pi}{4}ls^2$	$\pi s(l+\frac{s}{2})$	$\frac{4}{s}+\frac{2}{l}$
Spheres	$\frac{\pi}{6}s^3$	πs^2	$\frac{6}{s}$

surface area to unit volume ratios are reported for the three (ideal) typologies of particles as function of the characteristic dimension (s): thickness for disks ($d = 1$ μm), diameter for cylinders ($l = 1$ μm) and spheres. In Table 1.1 the relations used to calculate the ratios are listed. Some examples of the three kind of NPs are: graphene and clay are plate-like particles; carbon nanotubes and cellulose nanofibers are cylindrical; carbon black, silica and oligomeric sislesquioxanes (POSS) are almost spherical. Another important property arising from the small dimensions of NPs is related to the extension of the *interfacial region* to the entire bulk of the system. The interfacial region is defined as the part of the polymer matrix that is influenced by the presence of the filler, as farther parts are not affected by its presence. As this region usually extends only for few nanometers ($2 \div 10$ nm) for traditional composites, at low filler concentrations, only a reduced part of the matrix is influenced. In Figure 1.1e the average interparticle distance is reported for homogeneously dispersed spherical particles as function of the particle volume fraction. It can be seen that for very small particles the average interparticle distance is below 20 nm meaning that the whole matrix is influenced by the filler also at very low content.

One of the key limitations of the adoption of NPs is processing. In order to exploit the high surface area and the short average interparticle distance it is fundamental to reach an almost perfect state of both distribution and dispersion of the filler. The first is obtained when the system is homogeneous and the filler is found with the same probability within the whole volume; the second is reached when all agglomerates are broken and the particles are found in an isolated state. The distribution state is mainly related to

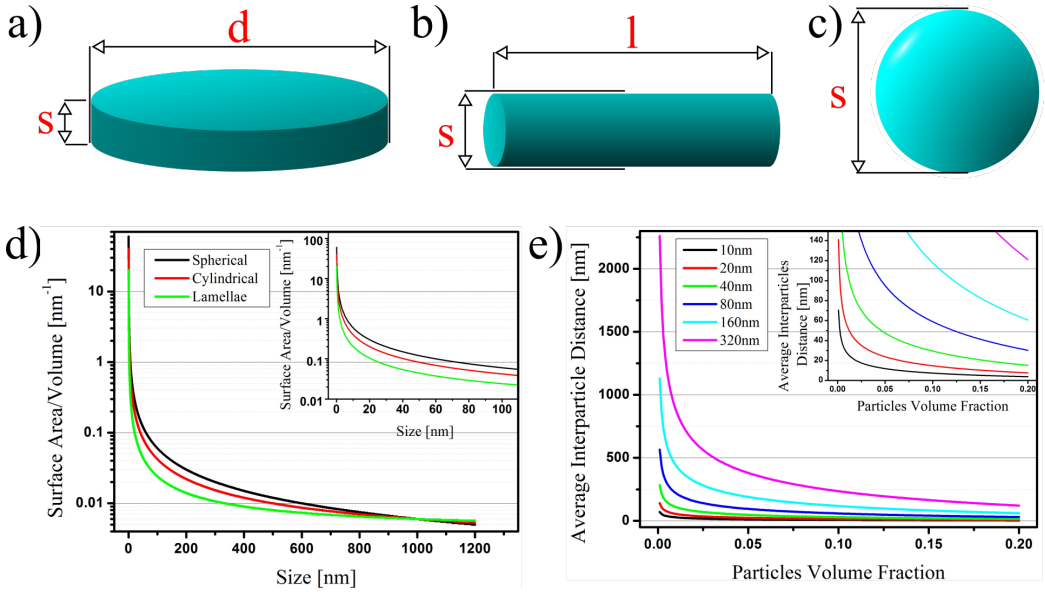

Figure 1.1: Schematic of nanoscale fillers presenting one (a), two (b) or three (c) dimensions below 100 nm. Surface area to volume ratio for particles as function of the smallest dimension. (d) Average distance between spherical NPs ideally dispersed in a matrix as function of the particles volume ratio. (e)

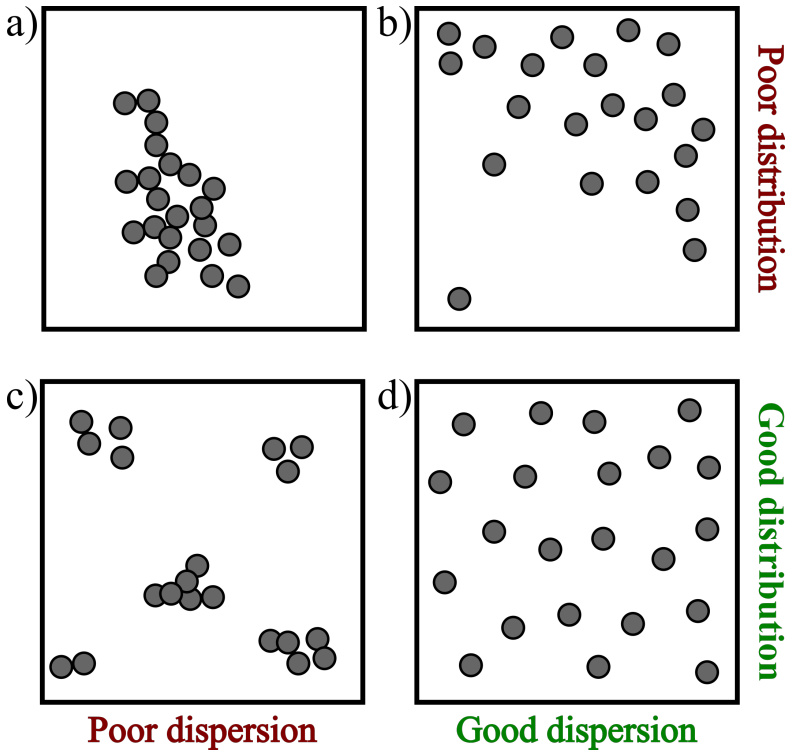

Figure 1.2: A schematic illustration of the difference between dispersion and distribution and giving examples of good and poor of each.

processing conditions and, for example, a longer mixing time can greatly improve it. The dispersion is otherwise related to the chemical interaction between the filler and the matrix. As the dimension of particles decreases the attractive forces arising from the Van der Waals interactions increase leading to the growth of the agglomerates. A proper formulation of the chemistry (e.g. through chemical modification of the particles) of the system can help reaching a good dispersion improving the interactions between the particles and the matrix. In Figure 1.2 a schematic illustration of the four possibility of dispersion and distribution state is given: poor distribution and dispersion (a), poor distribution and good dispersion (b), good distribution and poor dispersion (c), good distribution and dispersion (d).

Table 1.2: Characterization techniques sorted by typology.

Typology	Examples
Morphology	visible light microscopy
	scanning electron microscopy (SEM)
	transmission electron microscopy (TEM)
	scanning probe microscopy (SPM)
	scanning tunneling microscopy (STM)
	atomic force microscopy (AFM)
Spectroscopy	energy dispersive x-ray spectrometry (EDX or EDS)
	fourier transformed infra-red spectroscopy (FTIR)
	raman spectroscopy
	nuclear magnetic resonance (NMR)
Thermo-mechanical	differential scanning calorimetry (DSC)
	thermogravimetric analysis (TGA)
	thermomechanical analysis (TMA)
	dynamic mechanical analysis (DMA)
	rheometry
Structural	wide-angle X-ray diffraction (WAXD)
	small-angle X-ray scattering (SAXS)

Characterization techniques for nanocomposites

As remarkable progresses were made in the processing and commercialization of NCs these systems have become a crucial research field[2] and these materials were elected as best candidates for next-generation materials. [3] NPs possess unique properties, usually dependent on their size, from the point of view of the chemical, electrical, mechanical and photonic, that can be transferred to polymer matrix. [4, 5, 6, 7] For this reason characterization tools are crucial to analyse physical and chemical properties of NCs. [8] The most important characterization techniques can be categorised, as shown in Table 1.2, as: morphological, spectroscopic, thermo-mechanical and structural. Visible light microscopy is usually used to macroscopically analyse samples. It can give general and fast information about the morphology and the presence of macroscopic defect. Obviously it cannot be used to see anything that is below diffraction limit of every optical system (around 400 nm). The scanning electron microscopy (SEM) provides images of surface features associated

with a sample using the primary or the secondary electrons diffused by the sample when hit by a focused electron beam. [9] In a transmission electron microscope (TEM) the electron beam is transmitted through an ultra-thin slice of the sample obtained using a microtome. [10] The scanning probe microscope (SPM) gives images of the surface topology scanning the sample with a very sharp tip while a sensor acquires its movement. [11] The scanning tunneling microscope (STM) is very similar but the tip is conductive and so close to the sample (typically about 0.5 nm) that tunnel currents can flow across the gap. This method provides not only a topological information about the surface but also an analysis of the electronic bands of the system. [12] The limitation of an STM is that can work only with electrically conductive samples. A way to overcome to this limitation is to use an atomic force microscope (AFM) that measures the non-bonding forces between the sharp tip and the sample to obtain a high-resolution map of the sample in terms of the morphology or of the elastic modulus. [13]

For elemental analysis and the determination of the different phases in a nanocomposite, when the filler is not organic, spectroscopic analysis can be performed. Energy-dispersive X-ray spectroscopy is an analytical technique used to determine the elemental composition of a sample or of a part of it. [14] Infrared and Raman spectroscopy are used to obtain absorption and emission spectra of molecules activating their vibrational modes. The obtained spectra can be used to determine the structure of the molecules or to identify them due to the unique fingerprint represented in the spectrum. [15, 16] Another important characterization technique is the nuclear magnetic resonance spectroscopy used to obtain physical, chemical and structural information of molecules. It is based on the absorption and emission of electromagnetic radiation of materials in a strong magnetic field.[17]

For thermal characterization the most used characterization techniques are: the differential scanning calorimeter (DSC) [18], the thermogravimetric (TGA) [19], the thermomechanical (TMA) [20], the dynamic mechanical (DMA) [21] and the rheologic analysis[22].

Wide-angle X-ray diffraction (WAXD) is commonly used to determine the NC internal structure [23, 24] while small-angle X-ray scattering (SAXS) is

typically used to observe structures on the order of 10Å or more. [25]

Nanoparticles structuring

The amount of NPs available today is huge. In order to exploit the properties of these particles usually they must be implemented within a device, and then immobilised in the position in which they will perform their function. The ability to locate and fix the particles in the desired positions plays a key role in order to obtain new and performing devices. [26]

One of the main methods for particles immobilization is their additions into polymer matrices. [2] The possibility of using almost any type of polymer available today, thermoplastic or thermosetting, makes this area of vast interest and in constant growth. The inclusion of particles into the polymer can be achieved in different ways depending on the polymer type. For thermoplastic polymers with high molecular weight this is done by melt mixing or using an appropriate solvent. [27] The low molecular weight thermosetting polymer precursors are usually fluid at room temperature, and this allows to easily mix the particles before the step of polymerization or crosslinking. [28]

A very interesting strategy to structure the NPs, at the micro or nanoscale, is to structure the polymer containing them. In this way it is possible to transfer the large amount of existing, and standardised methods, used for polymer structuring to obtain the structuring of the particles. [29, 30]

The possibility of structuring on different length scales these materials has the combination of benefits arising from the different pore sizes. [31, 32] Meso and macroporous coexistence can provide a very high surface combined with an increased mass transport due to the easy access through the material. For such reasons these materials are very promising for sensor devices and catalysis. [33]

Nanomaterials can be also be used as ultra sensitive detection exploiting their unique chemical, physical and electronic properties that act as transducers when implemented into optical, electronic, chemical or mechanical devices. [34] Many different materials have been used for such a scope as metals, semiconductors, carbon and polymers to prepare nanomaterials such

as NPs [35, 36], nanotubes [37, 38] and nanowires [39, 40].

Many nano-structures have been, for example, studied for biosensing applications. [41, 42] Hierarchically structured NCs have been investigated as chemosensory materials. [43]

In the memory devices field a nonvolatile plastic nonvolatile digital memory based on nanofibers of polyaniline decorated with gold NPs was reported. The device was plastic composite film working between two electrodes using an external field to control it. [44]

In another case CdSe/ZnS quantum dots (QDs) were used in combination of electrospinning method in order to obtain nanocomposite fibers of PMMA with improved properties of thermal stability. [45]

One possible approach consisted in the production of a three-dimensional micro structured beam reinforced with single walled carbon nanotube (SWCNT) polymer NC fabricated using a microfluidic approach. The final sample consisted in a complex network of SCWNTs impregnated with a thermosetting resin leading to better mechanical performances under flexural solicitiations. [46]

Also in the research for new materials for batteries NCs have been adopted to improve the electrochemical performances of the lithium-ion batteries. The strategy relies on the production of a nanostructured electrode based on a mesoporous conductive polymer filled with nanocrystals. The nanoscale dimension of the crystals leads to the increase in the contact area between electrode and electrolyte, while the mesopores facilitate the transport of the electrolyte ions. [47]

The aim of this work is to explore three different methods for micro and nano- structuring of NPs into polymers. Each of this researches ended with the production of an article submitted or published on peer-reviewed international journals:

Phase separation *Double percolation of multiwalled carbon nanotubes in PS/PLA blends*, submitted to ACS Applied Materials and Interfaces (Chapter 2)

Instability in thin films *Patterning of perovskite-polymer films by wrin-*

kling instabilities, submitted to Soft Matter (Chapter 3)

Electrohydrodynamic *Dielectrophoretic assembly of quantum dots into PDMS microlenses*, published on IEEE Journal of Selected Topics in Quantum Electronics (Chapter 4)

References

[1] Pulickel M Ajayan, Linda S Schadler, and Paul V Braun. *Nanocomposite science and technology*. John Wiley & Sons, 2006.

[2] Farzana Hussain et al. "Review article: polymer-matrix nanocomposites, processing, manufacturing, and application: an overview". In: *Journal of composite materials* 40.17 (2006), pp. 1511–1575.

[3] RTO Lecture Series. *EN-AVT-129*. 2005.

[4] Shuwen Zeng et al. "A review on functionalized gold nanoparticles for biosensing applications". In: *Plasmonics* 6.3 (2011), pp. 491–506.

[5] Erik T Thostenson, Zhifeng Ren, and Tsu-Wei Chou. "Advances in the science and technology of carbon nanotubes and their composites: a review". In: *Composites science and technology* 61.13 (2001), pp. 1899–1912.

[6] Yaodong Liu and Satish Kumar. "Polymer/carbon nanotube nano composite fibers–a review". In: *ACS applied materials & interfaces* 6.9 (2014), pp. 6069–6087.

[7] Xianmao Lu et al. "Chemical synthesis of novel plasmonic nanoparticles". In: *Annual review of physical chemistry* 60 (2009), pp. 167–192.

[8] Meyya Meyyappan. *Carbon nanotubes: science and applications*. CRC press, 2004.

[9] Joseph Goldstein. *Practical scanning electron microscopy: electron and ion microprobe analysis*. Springer Science & Business Media, 2012.

[10] David B Williams and C Barry Carter. *The transmission electron microscope*. Springer, 1996.

[11] Bharat Bhushan and Othmar Marti. *Scanning probe microscopy–principle of operation, instrumentation, and probes*. Springer, 2010.

[12] C Julian Chen. *Introduction to scanning tunneling microscopy*. Vol. 2. Oxford University Press New York, 1993.

[13] Victor J Morris, Andrew R Kirby, A Patrick Gunning, et al. *Atomic force microscopy for biologists*. Vol. 57. World Scientific, 1999.

[14] Daisuke Shindo and Tetsuo Oikawa. "Energy Dispersive X-ray Spectroscopy". In: *Analytical Electron Microscopy for Materials Science*. Springer, 2002, pp. 81–102.

[15] Mildred S Dresselhaus et al. "Raman spectroscopy of carbon nanotubes". In: *Physics reports* 409.2 (2005), pp. 47–99.

[16] Guangming Chen et al. "FTIR spectra, thermal properties, and dispersibility of a polystyrene/montmorillonite nanocomposite". In: *Macromolecular Chemistry and Physics* 202.7 (2001), pp. 1189–1193.

[17] Edward Raymond Andrew. "Nuclear magnetic resonance". In: *Nuclear Magnetic Resonance, by ER Andrew, Cambridge, UK: Cambridge University Press, 2009* 1 (2009).

[18] Günther Höhne, Wolfgang F Hemminger, and H-J Flammersheim. *Differential scanning calorimetry*. Springer Science & Business Media, 2013.

[19] AW Coats and JP Redfern. "Thermogravimetric analysis. A review". In: *Analyst* 88.1053 (1963), pp. 906–924.

[20] GD Liang and SC Tjong. "Electrical properties of low-density polyethylene/multiwalled carbon nanotube nanocomposites". In: *Materials chemistry and physics* 100.1 (2006), pp. 132–137.

[21] L Priya and JP Jog. "Intercalated poly (vinylidene fluoride)/clay nanocomposites: structure and properties". In: *Journal of Polymer Science Part B: Polymer Physics* 41.1 (2003), pp. 31–38.

[22] Ernesto Di Maio et al. "Isothermal crystallization in PCL/clay nanocomposites investigated with thermal and rheometric methods". In: *Polymer* 45.26 (2004), pp. 8893–8900.

[23] P Reichert et al. "Nanocomposites based on a synthetic layer silicate and polyamide-12". In: *Acta Polymerica* 49.2-3 (1998), pp. 116–123.

[24] Kazuhisa Yano et al. "Synthesis and properties of polyimide–clay hybrid". In: *Journal of Polymer Science Part A: Polymer Chemistry* 31.10 (1993), pp. 2493–2498.

[25] Roy Shenhar, Tyler B Norsten, and Vincent M Rotello. "Polymer-Mediated Nanoparticle Assembly: Structural Control and Applications". In: *Advanced Materials* 17.6 (2005), pp. 657–669.

[26] Montserrat Colilla, Blanca Gonzalez, and Maria Vallet-Regi. "Mesoporous silica nanoparticles for the design of smart delivery nanodevices". In: *Biomaterials Science* 1.2 (2013), pp. 114–134.

[27] R Haggenmueller et al. "Aligned single-wall carbon nanotubes in composites by melt processing methods". In: *Chemical physics letters* 330.3 (2000), pp. 219–225.

[28] Peng-Cheng Ma et al. "Dispersion and functionalization of carbon nanotubes for polymer-based nanocomposites: a review". In: *Composites Part A: Applied Science and Manufacturing* 41.10 (2010), pp. 1345–1367.

[29] Hao Zeng et al. "Exchange-coupled nanocomposite magnets by nanoparticle self-assembly". In: *Nature* 420.6914 (2002), pp. 395–398.

[30] Andreas Walther, Kerstin Matussek, and Axel HE Muller. "Engineering nanostructured polymer blends with controlled nanoparticle location using Janus particles". In: *Acs Nano* 2.6 (2008), pp. 1167–1178.

[31] Tapas Sen et al. "One-Pot Synthesis of Hierarchically Ordered Porous-Silica Materials with Three Orders of Length Scale". In: *Angewandte Chemie* 115.38 (2003), pp. 4797–4801.

[32] Daibin Kuang, Torsten Brezesinski, and Bernd Smarsly. "Hierarchical porous silica materials with a trimodal pore system using surfactant templates". In: *Journal of the American Chemical Society* 126.34 (2004), pp. 10534–10535.

[33] Jianbo Lu et al. "Vapour sensing with conductive polymer nanocomposites (CPC): Polycarbonate-carbon nanotubes transducers with hierarchical structure processed by spray layer by layer". In: *Sensors and Actuators B: Chemical* 140.2 (2009), pp. 451–460.

[34] Hari Singh Nalwa. "Encyclopedia of nanoscience and nanotechnology". In: (2004).

[35] Caroline H Walker, John V St. John, and Patty Wisian-Neilson. "Synthesis and size control of gold nanoparticles stabilized by poly (methylphenylphosphazene)". In: *Journal of the American Chemical Society* 123.16 (2001), pp. 3846–3847.

[36] Benjamin Wiley et al. "Polyol synthesis of silver nanoparticles: use of chloride and oxygen to promote the formation of single-crystal, truncated cubes and tetrahedrons". In: *Nano Letters* 4.9 (2004), pp. 1733–1739.

[37] Sumio Iijima et al. “Helical microtubules of graphitic carbon”. In: *nature* 354.6348 (1991), pp. 56–58.

[38] Jun Chen et al. “Titanium disulfide nanotubes as hydrogen-storage materials”. In: *Journal of the American Chemical Society* 125.18 (2003), pp. 5284–5285.

[39] Youngjo Tak and Kijung Yong. “Controlled growth of well-aligned ZnO nanorod array using a novel solution method”. In: *The Journal of Physical Chemistry B* 109.41 (2005), pp. 19263–19269.

[40] Liang Liang et al. “Direct assembly of large arrays of oriented conducting polymer nanowires”. In: *Angewandte Chemie International Edition* 41.19 (2002), pp. 3665–3668.

[41] Santhisagar Vaddiraju et al. “Emerging synergy between nanotechnology and implantable biosensors: a review”. In: *Biosensors and Bioelectronics* 25.7 (2010), pp. 1553–1565.

[42] Tarushee Ahuja, Devendra Kumar, et al. “Recent progress in the development of nano-structured conducting polymers/nanocomposites for sensor applications”. In: *Sensors and Actuators B: Chemical* 136.1 (2009), pp. 275–286.

[43] Shengyang Tao et al. “Hierarchically structured nanocomposite films as highly sensitive chemosensory materials for TNT detection”. In: *ChemPhysChem* 7.9 (2006), pp. 1902–1905.

[44] Ricky J Tseng et al. “Polyaniline nanofiber/gold nanoparticle nonvolatile memory”. In: *Nano letters* 5.6 (2005), pp. 1077–1080.

[45] Suying Wei et al. “Nanoporous poly (methyl methacrylate)-quantum dots nanocomposite fibers toward biomedical applications”. In: *Polymer* 52.25 (2011), pp. 5817–5829.

[46] LL Lebel et al. “Three-dimensional micro structured nanocomposite beams by microfluidic infiltration”. In: *Journal of Micromechanics and Microengineering* 19.12 (2009), p. 125009.

[47] C Lai et al. “Mesoporous polyaniline or polypyrrole/anatase TiO 2 nanocomposite as anode materials for lithium-ion batteries”. In: *Electrochimica Acta* 55.15 (2010), pp. 4567–4572.

Chapter 2

Double percolation of multiwalled carbon nanotubes in PS/PLA blends

2.1 Introduction

Both theoretical models and experimental measurements have revealed that carbon nanotubes (CNTs) possess outstanding mechanical and electrical properties. CNTs have been already incorporated into commercial composites and many works about their processing can be found in literature. Nevertheless many issues remain to be solved about dispersion, agglomeration during bulk processing and purification. In particular clumps and agglomerates formation of single walled and multi walled carbon nanotubes (SWCNT and MWCNT) can affect dramatically the performances of the nanocomposite (NC) because those represent defect sites that will trigger the breakage acting due to the stress concentration phenomenon.[1] The quality of dispersion is also related to the quality and purity of the nanoparticles. MWCNTs synthesised using the chemical vapour deposition (CVD) method, that produces much more pure particles, showed much better dispersion and increase of modulus and strength [2] showed compared to composite of polystyrene and arc-discharge-grown MWCNTs [3]. The most common method to achieve a good dispersion of nanotubes is by means of sonication in solvents as N,N-dimethylformamide (DMF), N-Methyl-2- pyrrolidone (NMP), cyclopentane,

and e-caprolactone that are strong Lewis bases without hydrogen donors. This approach is not always suitable therefore different strategies can be adopted to improve the interaction between particles and the dispersing matrix. Stable suspensions can be obtained with the aid of surfactants[4], alkyl or carboxyl terminated groups [5], aliphatic amines [6] or fluorine[7]. Surface functionalization should be used carefully because it can lead to mechanical or functional loss of properties and can dramatically affect the properties of the final composite.[8, 9]

In a NC obtained by a solvent assisted process the polymer should be soluble in the solvent in which the CNTs are dispersed and then dried out. This approach is not suitable for large-scale production so the aim of the functionalization could be the improvement of the interaction of the filler with the polymer in the liquid state, at high temperatures for thermoplastic polymers or before the crosslinking for thermosetting polymer. [10, 11, 12, 13] For melt mixed NCs the dispersion is improved due to the great amount of mechanical energy supplied by the rotating screws. This extra energy is used to overcome the interactive Van der Waals forces holding the CNT bundles togheter.[14] In some cases this extra energy is not enough to break the agglomeration due to the very weak affinity of the filler and the polymer, in those cases the CNTs functionalization is mandatory.

Melt mixing of two or more different polymers lead to different morphologies depending on the rheological and thermodynamic properties of the phases and on processing conditions. The morphology developed during the mixing strongly influences the final properties of the system. Four basic morphologies can be formed at the end of the process:

- Inclusion into the majority phase
- Fibers into the majority phase
- Planar alternating phases (lamellae)
- Bicontinuous phases (or co-continuous)

The first category is the most commonly found in commercial polymer blends as this is the most commonly obtained in a very large range of compositions.

The least common is the bicontinuous morphology that is attracting more and more interests due to the peculiar properties that can offer. The elastic moduli were found much higher in values for bicontinuous blends when compared to the same blends in a inclusion/matrix dispersion.[15] Also electrical conductive blends revealed very benefits arising from the bicontinuous morphology, as the possibility of selectively localize the conductive filler can lead to a sensible decrease of the electrical percolation threshold. [16]

The conditions that lead to the formation of bicontinuous morphologies are still not well clear. Depending on the shape of the inclusion of the minority phase into the other, a continuous phase can be obtained also at low concentration. However in this condition not all the minor phase participate to the formation of the continuous network and some part of it is still in the form of inclusion in the majority phase. The condition at which a full bicontinuous morphology is obtained are not completely defined.[17] One possible mechanism is the spinodal decomposition that lead to the formation of a bicontinuous structure but this is an exception in melt mixed polymer blends as the majority of polymer have not a miscibility a miscible region due to thei high molecular weights. Another way of obtained co-continuous structures at the level of the polymer chains is by the synthesis of interpenetrating newtworks (IPN). [18, 19] Those systems fall under the first of the two possible definition of co-continuous structures. The first is defined as the *coexistence of at least two continuous structures within the same volume.* This definition has no restrictions on the scale of mixing and on the structure formed. In literature co-continuous structures, satisfying this definition are also called:

- thermoplastic IPNs
- IPNs of phases
- interpenetrating co-continuous phase structure
- interpenetrating phase structures (IPSs)
- interpenetrating polymer blends (IPBs)

The second definition was proposed by Lyngaae-Jørgensen and Utracki and states that a morphology is defined bicontinuous when *at least a part of each phase forms a continuous structure within the whole volume.*[20] According to this definition before the transition point the system presents only discrete domains of one phase dispersed in the other continuous phase. At the transition point the first phase forms an infinite continuous phase but some part of it can still maintain some discrete domains. This transition point is called critical volume fraction (c_r). When all the discrete domains join the continuous network for all the phases a fully co-continuous morphology is achieved. When the bicontinuity is reached in a binary blend the two phase are topologically complement also defined as *antitropic*. The continuity index Φ_I represents the portion of a component that is part of the percolating structure. To measure the continuity index one of the phases is extracted using an orthogonal solvent that can selectively dissolve one phase leaving intact the other one. The difference in weight before and after the extraction indicates the amount of the extracted phase that was part of the continuous network. Discrete domains cannot be removed from the system because they are screened by the non-soluble phase. If the bicontinuous index, of one of the phases, is close to 1 it means that no discrete domains, of that phase, are still present in the system. The two definition are not so different one from the other and, when the bicontinuous index is equal to 1 for all the phases, the two definitions coincide. For this reason the first definition can be seen as a special case of the second one.

The most effective way of obtaining a full bicontinuous system is the intensive melt mixing of two polymer in equivolume and equiviscous conditions (same volume fraction and same viscosity). Because not always this conditions are possible or desired a precise verification of the process condition need to be performed. The phase with the lower viscosity tend to be continuous because this minimize the total energy dissipation of the system, for this reason the viscosities of the two polymers should be compensate. [21]

Many researchers have reported that the addition of a nanofiller can affect the interfacial energies of multiphase system. This phenomenon can occur due to two different mechanisms. The first one is a mechanism of *ther-*

modynamic compatibility when the nanoparticles are miscible or compatible with both phases. The total free-energy of mixing (ΔG_{mix}) becomes negative and the two components becomes compatible due a thermodynamically driven compatibility. The second mechanism is the *dynamic compatibility* and happens when the fille is mainly dispersed in the component with lower viscosity or polarity. This localization changes the viscosity and prevents the coalescence of the domains.[22]

The selective localization is for this reason a very interesting mechanism to exploit to obtain materials with improved performances. At the base of a selective dispersion of a filler in a multiphase system is the higher affinity of the anisotropic particles with one of the phases during the melt mixing. The interaction between the particles and each one of the two phases depends on the surface energies of the three components. The filler located in the component with the lower viscosity can reduce this viscoelastic difference and contribute to the breakup of the droplets. For this reason a proper choice of the filler is crucial to reach the desired dispersion. The equilibrium localization of the particles at equilibrium condition can be estimated using Young's equation calculating the wetting coefficient:[23]

$$\omega = \frac{\sigma_{\text{NP-B}} - \sigma_{\text{NP-A}}}{\sigma_{\text{A-B}}} \tag{2.1}$$

where $\sigma_{\text{i-j}}$ is the interfacial energy between the component i and j. If the wetting coefficient is higher than $+1$ the filler is located in the phase A, in the phase B if lower than -1 and localized at the interface of $\text{A} - \text{B}$ if comprised between -1 and $+1$. The wetting coefficient has been shown to be successfully used in systems where the polar difference between the two polymers is sufficiently high.[24] Thermodynamyc aspects are not the only factors influencing the final dispersion and morphology of the nanocomposite. For this reason also kinetic aspects such as the viscosities or the process condition should be taken into account.

Many works has tried to exploit the advantages of selective localization of fillers to improve the properties of the final material. In 2011 Wu *et Al* prepared a poly lactic acid (PLA) and polycaprolactone (PCL) blend containing

organoclay as filler and characterized the effect of selective localization on different properties as the crysallization and the perfomances.[25] In 2004 Li *et Al* analysed the morphology of a poly(phenylene oxide) (PPO) and polyamide 6 (PA6) blend with various amounts of organically modified clay. They found that the selective localization of exfoliated clay in the PA6 phase increased and also impeded the coalescence of the PPO phase.[26] Wode *et Al* conducted preliminary experiment to check the affinity of functionalized MWCNTs with polystyrene (PS) and poly(2-vinylpyridine) (P2VP) and selectively sequestering them in each of the two phases of a PS-b-P4VP block copolymer.[27] Another work on selective localization of MWCNTs was conducted by Göldel *et Al* in 2008 either using a two step procedure to incorporate the filler in one phase of a polycarbonate (PC)/poly(styrene-acrylonitrile) (SAN) blend or mixing the three components together at the same time.[28]

2.2 Article

2.2.1 Authors and affiliations

- Giuseppe Nasti[a,b]
- Gennaro Gentile[b,*]
- Pierfrancesco Cerruti[b]
- Cosimo Carfagna[b]
- Veronica Ambrogi[a]

[a] Department of Chemical, Materials and Production Engineering, University of Naples "Federico II", Piazzale Tecchio 80, 80125 Napoli, Italy.

[b] Institute for Polymers, Composites and Biomaterials (IPCB-CNR), via Campi Flegrei 34, 80078 Pozzuoli (Na), Italy.

[*] Corresponding author

2.2.2 Introduction

Blending different polymers is a common strategy in order to modulate or improve the properties of a polymeric material or to introduce new properties. [29] Due to the high molecular weight, achieving compatibility and miscibility of polymers is not a trivial task. In most cases, the mixed polymers undergo phase separation, since reducing interfacial area leads to minimization of the system free energy. The morphologies of phase separated immiscible polymer blends can be divided into four categories: 1) globular inclusions (of the minor phase) in a continuous matrix, 2) fibers (of the minor phase) in a continuous matrix, 3) alternating superimposed lamellae of the two phases, and 4) bicontinuity. [30, 31, 21] Great interest has the bicontinuous morphology, which is characterized by the formation of two connected and continuous complementary phases within the whole volume of the material. In such a morphology it is not possible to define a majority phase in which the minority phase is included. The main strategy used to determine the formation of a bicontinuous morphology is selective extraction of a phase. With the use of an orthogonal solvent is possible to selectively extract one of the two

phase leaving intact the other one, and forming a porous self- standing structure. From the weight difference measured before and after extraction the bicontinuity coefficient Φ can be calculated: [32]

$$\Phi = \frac{w_i - w_f}{\phi w_i} \tag{2.2}$$

where w_i and w_f are the respectively the initial and final weight of the sample, ϕ is the weight ratio of the extracted phase. If the sample after the extraction maintains a self-standing structure, and the value of Φ is close to unity, then the material is bicontinuous. Only internal regions of the extracted phase connected to the surface are available to the solvent for the extraction. After the extraction a macro-porous material is formed, with connected pores usually in the dimension range of 1-100 μm

Another important technological aspect regarding polymer blends is the addition of fillers, with the aim of reducing total cost or imparting properties to the materials. Nanocomposites belong to this last category. Nanosized particles with some specific property can be added in small amount to one or more polymer during mixing in order to confer that property to the final composite. For multiphasic immiscible blends, the addition of nanoparticles can lead to very interesting results. These fillers can show an affinity with one of the components of the blend, tending to concentrate selectively into one of the phases or at the interface between two phases. [33, 34, 35, 36]

Among all the other particles carbon nanotubes (CNT) possess many interesting properties (e.g. elastic modulus, tensile strength, electrical conductivity). Under the right conditions, CNT dispersion in a polymer matrix can lead to an improvement of elastic modulus or give new functional properties. When the amount of CNT filler in the polymer matrix is enough to create a percolated network within the whole volume of the material, then the polymer can show an increase in electrical conductivity of several orders of magnitude. Nanocomposites based on single walled (SWCNT) and multi walled (MWCNT) carbon nanotubes deserve great interest. CNTs are characterized by high form factor ($10^3 \div 10^5$), high electrical conductivity (10^6 S/m), similar to copper, [37] theoretical Young modulus and tensile

strength of 4 TPa and 220 GPa [38] The coincidence of all these astonishing properties allows to obtain higher electrical and mechanical performance improvements compared to those obtained using other particles (e.g. CB).

The dispersion state of the nanoparticles in the polymeric matrix is of fundamental importance in order to impart these properties to the final material. To this aim, it is necessary to counterbalance the attraction energy between particles due to Van der Waals interaction. [39, 40, 41] For these systems, a concentration percolation threshold is defined that is the critical concentration of nanoparticles that leads to the formation of a continuous network within the material. When this critical concentration is reached, most or all the properties of the material show a step-like variation. The percolation threshold is shown as being inversely related to the form factor of CNTs, and is strictly related to the dispersion state of the particles. [42, 43, 44] It is possible to demonstrate that for a generic property of the material σ (e.g. electrical conductivity) the following law is true: [45]

$$\sigma = \sigma_0(p - p_c)^t \tag{2.3}$$

where σ_0 is a scale factor dependent on the nature of the nanoparticles, p is the volume fraction of filler, p_c is the percolation threshold and t is the critical exponent. Theoretical calculations for cylindrical particles state that the minimum value for percolation threshold should be around 0.05 vol%. [14, 46]

Thresholds of 0.04 wt% have been reported for an epoxy resin/MWCNT [47, 48] and 0.05 wt% for a polypropylene (PP)/MWCNT blend. [49] Except for these examples, the typical percolation threshold values found in literature are comprised between 1 and 5 wt%. [50] Thanks to computer assisted calculations Kirkpatrick [51] and Balberg [52] valuated that the critical exponent should be equal to 1.3 for bi- dimensional systems and to 2 for tri-dimensional systems. In spite of this, much more scattered values of the critical exponent, between 1 and 10, are found in literature. [53]

The final properties of the nano-composites are strictly related to the dispersion state of the filler. When two or more polymers are mixed together,

specific interactions between particles and polymer components could result in particles to accumulate in one phase or to localize at the interface. This behaviour depends on the system thermodynamics (i.e. relative wettability) as well as on kinetic factors (i.e. mixing parameters). In equilibrium conditions, the localization of the filler will be driven by the minimization of the energy. To predict the final position of the particles, a wettability coefficient can be calculated, defined as: [54]

$$\omega = \frac{\gamma_{BC} - \gamma_{AC}}{\gamma_{AB}} \tag{2.4}$$

where γ is the interfacial energy between components, A and B representing the two polymers and C the filler. The value of ω determines which is the equilibrium position of the nanoparticle. If $\omega > 1$, particles will be localized in the phase A; if $\omega < -1$ in phase B; otherwise if $-1 < \omega < 1$, the interface will be the preferred region of dispersion. To calculate the $\gamma_i j$ interfacial energy, two different approaches are possible. [55] For high surface energy material the mean harmonic approximation is used:

$$\gamma_{ij} = \gamma_i + \gamma_j - 4\left(\frac{\gamma_i^d \gamma_j^d}{\gamma_i^d + \gamma_j^d} + \frac{\gamma_i^p \gamma_j^p}{\gamma_i^p + \gamma_j^p}\right) \tag{2.5}$$

while for low surface energy materials the geometric mean approximation holds:

$$\gamma_{ij} = \gamma_i + \gamma_j - 2\left(\sqrt{(\gamma_i^d \gamma_j^d)} + \sqrt{(\gamma_i^p \gamma_j^p)}\right) \tag{2.6}$$

In both equations, γ^d and γ^p are respectively the dispersive and polar components of surface energy of the components.

In 1991, Sumita et al introduced for the first time the concept of double percolation [23], for multiphasic nanocomposites for which the following conditions are satisfied at the same time: 1) uneven distribution of the filler in the phases; 2) achievement of the percolation threshold in one of the phases; 3) structural continuity of the percolated phase within the whole volume of the material. If all these conditions are satisfied the material is defined *double percolated*. The interest in double percolated systems lies on the need of

much lower filler concentration, on the total volume, to reach high performance (e.g. electrical conductivity). [56, 57, 58]

In this work we present the selective localization of MWCNT in PLA/PS bicontinuous blends. We prepared a masterbatch of PS with 2 wt% content of MWCNT, which was melt mixed with different amounts of PLA. Thanks to this two-step process we obtained a double percolated morphology where the MWCNT percolate the PS phase, forming a co-continuous network together with PLA. Scanning electron microscopy (SEM) and transmission electron microscopy (TEM) were used to verify respectively the formation of a bicontinuous morphology and the selective dispersion of the filler. To better analyse the morphology, the PS phase was selectively extracted by immersion in hot cyclohexane. Double percolation led to a very low electrical percolation threshold of about 0.45 vol% MWCNT on the total volume.

2.2.3 Experimental

Materials

PS (Edistir 2982) was purchased from Polimeri Europa (Italy), PLA was the 2002D grade from Na-tureworks (Minneapolis MN, USA). MWCNT grown by chemical vapor deposition (nominal purity $> 95\%$) were purchased from Cheap Tubes Inc. (Brattleboro VT, USA). Their diameter was between 30 and 50 nm.

Sample preparation

PS/PLA blends at different composition (20/80, 30/70, 40/60, 50/50, 60/40 and 70/30 PS to PLA weight ratio) were prepared introducing proper amounts of PS and PLA in the chamber (15 cm^3) of a twin-screw microcompunder (DSM Xplore MC15). Mixing was performed at 180 °C for 5 min, at the speed of 150 rpm, under an inert nitrogen atmosphere in order to protect polymer from degradation.

In order to obtain a double percolated system a two-step process was chosen. In the first phase, three different masterbatches of polystyrene, charged with 1, 2, or 6 wt% MWCNT were prepared in a 50 cm^3 blending chamber of

a two-roll Brabender Plastograph mixer at 180 °C for 10 min, under an inert nitrogen atmosphere. Compression molded disks (1 mm thick) were obtained from the different blends by compression molding at 180 °C for 10 min using a P200E bench top press (Dr Collin GmbH, Ebersberg, Germany) progressively increasing the pressure up to

The system containing 2 wt% of MWCNT (coded as PS2CNT) was chosen as reference masterbatch since this was the minimum content of MWCNT leading to electrical percolation (see 2.2.3 Electrical conductivity). Therefore, PS2CNT was used to produce blends with PLA (20/80, 30/70, 40/60, 50/50 and 60/40 PS2CNT to PLA weight ratio). Mixing of PS2CNT with PLA was performed at 180 °C for 5 min at 150 rpm under nitrogen using the DSM Xplore MC15 twin-screw microcompounder.

Rheological measurements

Melt rheological properties of PLA, PS and PS2CNT were measured using a Thermo Scientific Rhe-oStress 6000 rotational rheometer at 180 °C under nitrogen. Circular disks of 25 mm diameter obtained from granules were placed between parallel plates setting a gap of 1 mm. Frequency sweep analysis was performed in a 0.1 to 100 rad/s range (backward and forward) in the linear viscoelastic regime, with a constant stress of 50 Pa.

Bicontinuity coefficient

The bicontinuity coefficient was evaluated selectively removing the PS phase using hot cyclohexane. Samples of about 1 g were weighted and then immersed in vials containing cyclohexane at 60 °C for 24 h. Afterwards, the samples were put in an oven at 70 °C, under vacuum, for 24 h in order to remove the residual solvent, and then weighed again. This procedure was repeatedly performed until constant weight was reached (or until the loss of structural resistance), and the bicontinuity coefficient was calculated as in Equation 1. Measurements were performed in triplicate.

Morphology and selective localization of MWCNTs

The formation of a bicontinuous morphology was verified performing SEM analysis of extracted samples. Extruded strands of the melt mixed samples were cryo-fractured and then subject to solvent extraction as above described. SEM analysis was performed on a FEI Quanta 200 FEG SEM in high vacuum using a secondary electron detector and an acceleration voltage ranging from 10 to 30 kV. Before analysis, samples were coated with a 15 nm thick Au/Pd layer with a sputter coating system. Dynamic temperature-controlled SEM experiments were carried out on the above mentioned SEM using a hot stage and a gaseous secondary electron detector (GSED) at 30 kV acceleration voltage and $P_{H_2O} = 0.90$ torr. During SEM observation, samples were heated from room temperature to 140 °C (heating rate 50 °C/min). The selective localization of MWCNT in the polymer blend was evaluated by TEM analysis. Ultrathin sections of selected non-extracted samples were obtained with a Leica UC7 ultramicrotome system operating at room temperature. The sections were then placed on copper grids and observed in bright field mode on a FEI Tecnai G12 Spirit Twin TEM operating at 120 kV acceleration voltage.

Electrical conductivity

Volume conductivity measurements were performed using a Keithley Electrometer/High resistance meter (Model 6517A) coupled with the Resistivity Test Fixture (Model 8009). In particular, circular disks (6 cm diameter and 1 mm thickness) were obtained from the different blends by compression molding at 180 °C for 10 min using a P200E bench top press (Dr Collin GmbH, Ebersberg, Germany). The disks were then placed between the test fixture electrodes and the conductivity was measured using an alternating voltage between −10 V and +10 V, switching from positive to negative potential every 30 s. The conductivity was measured 8 times for each sample discarding the highest and the lowest measures.

2.2.4 Results and discussion

Rheology

The formation of bicontinuous domains during polymer melt mixing depends on the ratio of viscosities at the adopted processing condition, for a given volume ratio. As demonstrated by Pötschke and Paul [21], a bicontinuous morphology is formed when the following equation is satisfied, under certain assumptions:

$$\frac{\phi_i \eta_j}{\phi_j \eta_i} \approx 1 \tag{2.7}$$

where ϕ are the volume fractions of the polymers and η are the viscosities. In general, to obtain a bicontinuous morphology at a low volumetric content of one of the polymers, a high viscosity ratio is needed. For this reason, rheological tests were performed on neat PS and PLA, as well as on the PS/2CNT masterbatch. In Figure 2.1(a), the viscosities of PS, PLA and PS/2CNT are reported. The complex viscosity of PLA showed a clear Newtonian plateau at low shear rates. It is clearly visible that complex viscosity is increased for the PS2CNT sample compared to neat PS. While PS almost reached the Newtonian plateau, PS2CNT showed a mixed viscoelastic/solid-like behavior suggesting that the MWCNTs network was not completely formed. In Figure 2.1(b), the elastic and dissipative moduli are reported. The crossover between elastic and dissipative moduli for PLA occurs at $\sim$25 s^{-1} with a wide Newtonian plateau at low frequencies. A completely different behavior is shown by PS with a very short plateau and a much lower crossover frequency at $\sim$1 s^{-1} that shifts to $\sim$0.5 s^{-1} for the PS2CNT sample, due to the starting transition to a less dissipative system at low frequencies. [59] From these data we could estimate that phase inversion could occur at 60 wt% of PS. The prevision is made approximating the shear rate, expressed in s^{-1} , experienced by the polymers during the mixing with the velocity of twin screws, expressed in rpm ($\sim 10^2$ s^{-1}), as proposed by Wu in 1987. [60]

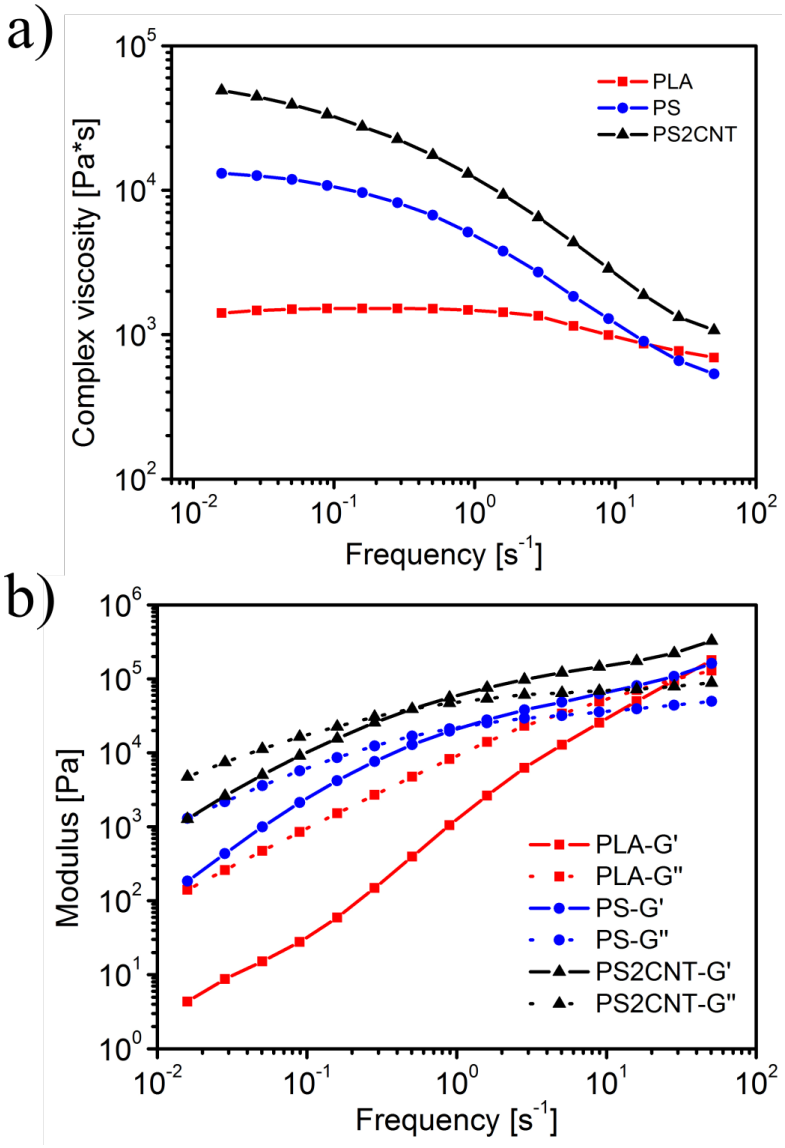

Figure 2.1: Complex viscosities (a), elastic and dissipative moduli (b) of PLA, PS and PS2CNT as a function of frequency at 180 °C.

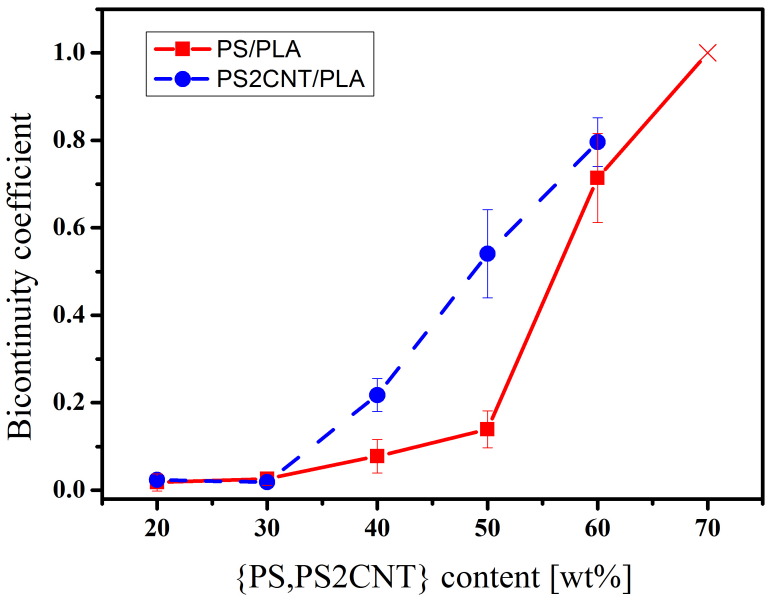

Figure 2.2: Bicontinuity coefficient for PS/PLA and PS2CNT/PLA blends after selective extraction of PS and PS2CNT phase in warm cyclohexane.

Bicontinuity coefficient

Extracting one of the phases is a peculiar characterization technique for bicontinuous blends. As both polymers are continuously connected within the whole volume of the material, a selective solvent can extract completely one of the two phases. Through weight measurements performed before and after extraction it is possible to determine if a bicontinuous morphology is formed. In Figure 2.2 we notice that the bicontinuity coefficient of the PS/PLA (Figure 2.2, red line) system starts to change at 40-50 wt% of PS, going from zero to 0.1, and then abruptly increases to 0.7 at 60 wt% of PS. It is worth to be noted that for the 70 wt% sample, complete loss of structural integrity was recorded after extraction, so that this point should not be taken into account. The PS2CNT/PLA blends showed a linear increase of bicontinuity from 30 wt% to 60 wt% (Figure 2.2, blue line).

Morphology

Selective extraction allowed to determine the obtained morphology from SEM imaging. In Figure 2.3, SEM images of PS/PLA blends at different weight fractions, namely 40/60 (Figure 2.3(a, b)), 50/50 (Figure 2.3(c, d)), and 60/40 (Figure 2.3(e, f)) are reported. It is possible to notice that the average size of PS cavities is almost constant (in the range $2 - 5$ μm), whereas the PLA domain dimension decreases as the PS weight fraction increases.

Then we proceeded to verify the effective localization of MWCNT in the blends prepared with the PS2CNT masterbatch. As stated above, it should be possible to predict, through the evaluation of the wettability coefficient, which is the more favorable phase for the nanoparticles. For the PS/PLA/MWCNT ternary system the wettability coefficient is calculated using Equation 2.4, where A is PS, B is PLA and C are MWCNTs. In 2.1 different literature values of surface energies of the three phases are reported. These values have been obtained at room temperature, except for PS_2 and PS_3, measured at 180 °C. It is noticed that significantly different values for polar and dispersive components of the surface energies are reported by different authors. Moreover, polar and dispersive components show a strong variation with temperature and values for different temperatures are hardly available, therefore it is difficult to choose a proper set of surface energies to calculate the wettability coefficient. For this reasons, in Table 2 the wettability coefficient was calculated for any possible combinations of data from Table 2.1, for both harmonic and geometric approximations (Equations 2.5 and 2.6). All the values smaller than -1 are reported in red, indicating that MWCNTs should prefer the PLA phase; the only value between -1 and $+1$ is reported in black, suggesting that the particles should localize at the PS/PLA interphase; all the values bigger than $+1$ are reported in green, indicating PS as the favorite phase for the nanotubes. It is clear that this calculation is strongly dependent on the set of values chosen.

In spite of the largely scattered values of wettability coefficients, TEM images in Figure 2.4(a, b) clearly show an asymmetrical distribution of MWCNTs. We can notice that MWCNT are present in PS (dark areas) and not in

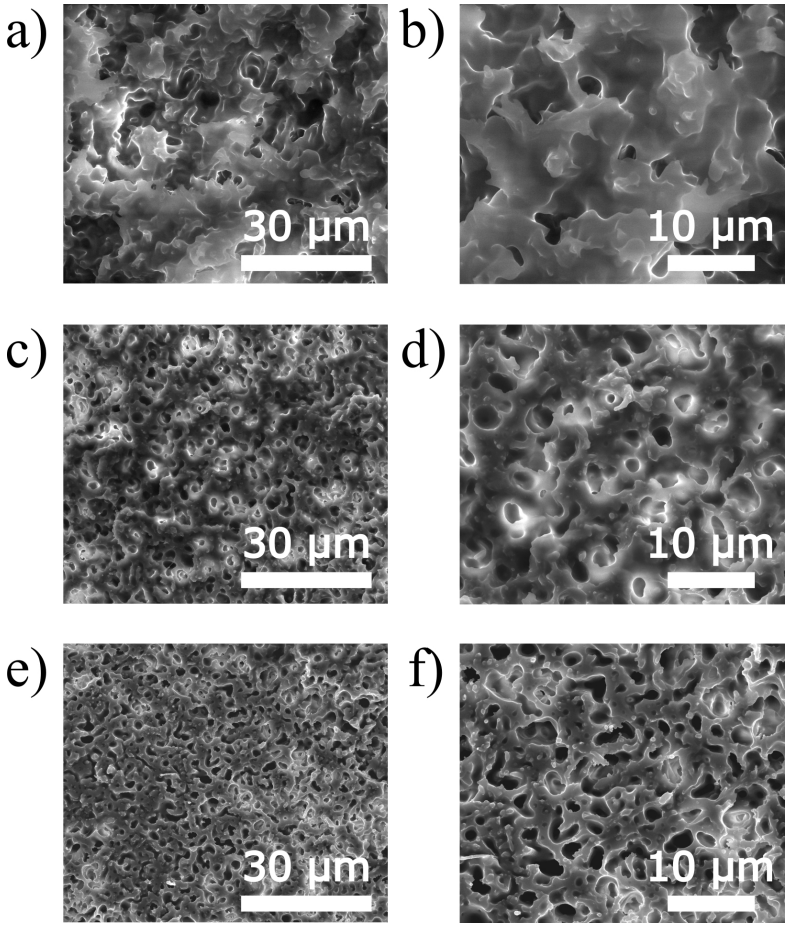

Figure 2.3: SEM micrographs of the bicontinuous morphology of selectively extracted PS/PLA blends at different weight fractions (PS/PLA: a, b = 40/60, c, d = 50/50, e, f = 60/40).

Table 2.1: Dispersive and polar surface energy coefficients for PS, PLA and MWCNTs.

	γ^d [mJ/m^2]	γ^d [mJ/m^2]	γ^d [mJ/m^2]	**Ref.**
PLA$_1$	39.6	3.9	43.5	[61]
PLA$_2$	36.6	0.0	36.6	[61]
PLA$_3$	29.7	10.5	40.2	[62]
PS$_1$	40.1	0.6	40.7	[61]
PS$_2$	32.5	8.1	40.6	[63]
PS$_3$	33.9	6.8	40.7	[63]
MWCNT	18.4	26.9	45.3	[64]

Table 2.2: Harmonic and geometric approximation for wettability coefficient of PS/PLA/MWCNT blends. Wettability values above +1 (green) are obtained when PS is the energetically preferred phase for MWCNTs, values below -1 (red) indicate PLA as the preferred phase for the nanotubes, and the value between -1 and 1 accounts for nanoparticles which tend to segregate at the interphase.

	Harmonic			**Geometric**		
	PLA_1	**PLA_2**	**PLA_3**	**PLA_1**	**PLA_2**	**PLA_3**
PS_1	-3.42	-0.37	-2.25	-6.46	+9.35	-2.69
PS_2	+5.03	+2.27	-9.54	+6.18	+2.74	-10.68
PS_3	+6.79	+2.37	-6.30	+8.57	+3.06	-7.17

PLA (bright areas). Although the mixing time has a relatively long duration, MWCNTs remain segregated in the PS phase, in which they were originally incorporated, and PLA remains almost completely free of particles. In order to get further insight on this finding, we prepared a PLA masterbatch containing 2 wt% MWCNTs. We mixed this masterbatch with PS in a 50/50 weight ratio. As clearly visible in TEM images in Figure 2.4(c, d), a great amount of particles moved during the melt mixing from the starting PLA phase to PS, even if this process does not lead to the complete asymmetry obtained using the PS2CNT masterbatch. These two experiments suggest the presence of a strong affinity of MWCNTs with PS, responsible for a thermodynamic force driving the particles from PLA to PS, or keeping them into PS. Moreover, another interesting behavior is the partial accumulation of MWCNT at the PS/PLA interface for the PS2CNT/PLA system, as shown in Figure 2.4(e, f) for PS2CNT/PLA. This can be due to a blocking effect of the interface during the diffusion of the particles. The force arising from the concentration gradient that should favor diffusion of the particles into PLA is balanced by the opposite force due to the stronger affinity with PS. In Figure 2.5 it is also shown that PS inclusions in PLA phase incorporate a considerable number of nanotubes compared to the surrounding matrix. In conclusion, all these data suggest a much stronger affinity of MWCNTs for the PS phase.

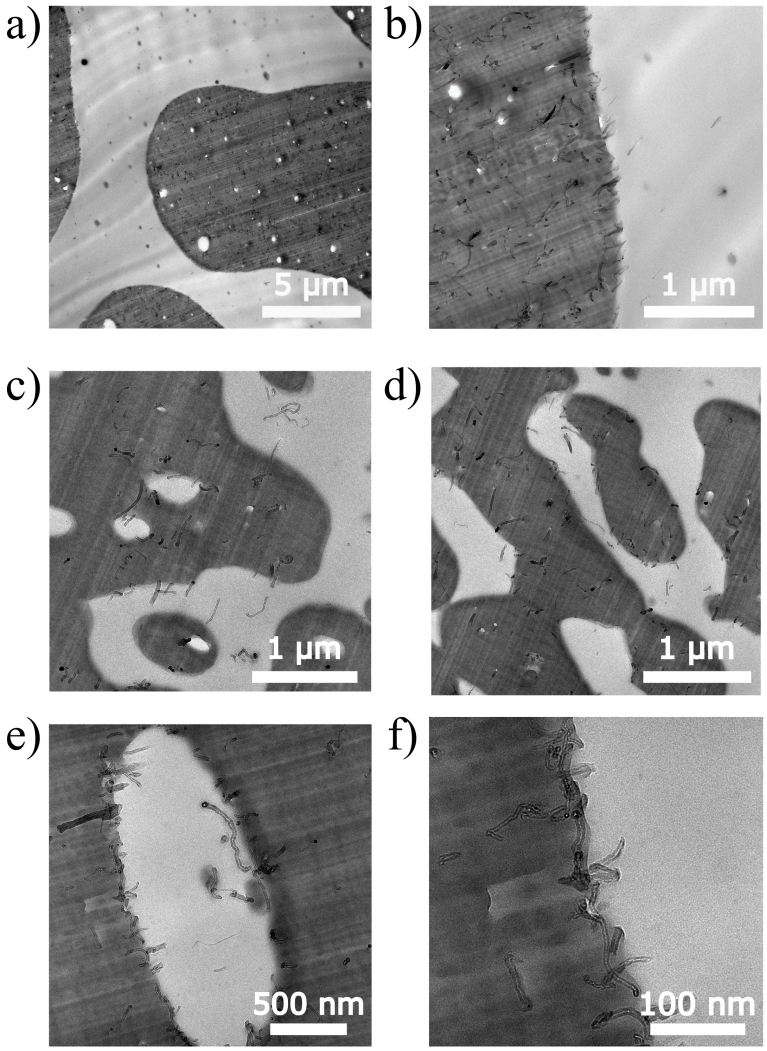

Figure 2.4: (a,b) TEM images of the 50/50 weight ratio PS2CNT/PLA blend, showing the asymmetric dispersion of MWCNTs in the PS phase. The dark phase (PS) contains almost all the MWCNTs while few isolat-ed particles are visible in the clear phase (PLA). (c, d) TEM images of PLA2CNT masterbatch melt mixed with PS in a 50/50 weight ratio. It is clearly shown that a great amount of MWCNTs migrate from the starting PLA phase (bright areas) to the PS (dark areas) during processing. (e, f) TEM images of the 50/50 PS2CNT/PLA blend, showing the accumulation of MWCNT stopped at the PS/PLA inter-face during the migration from the PS phase to PLA.

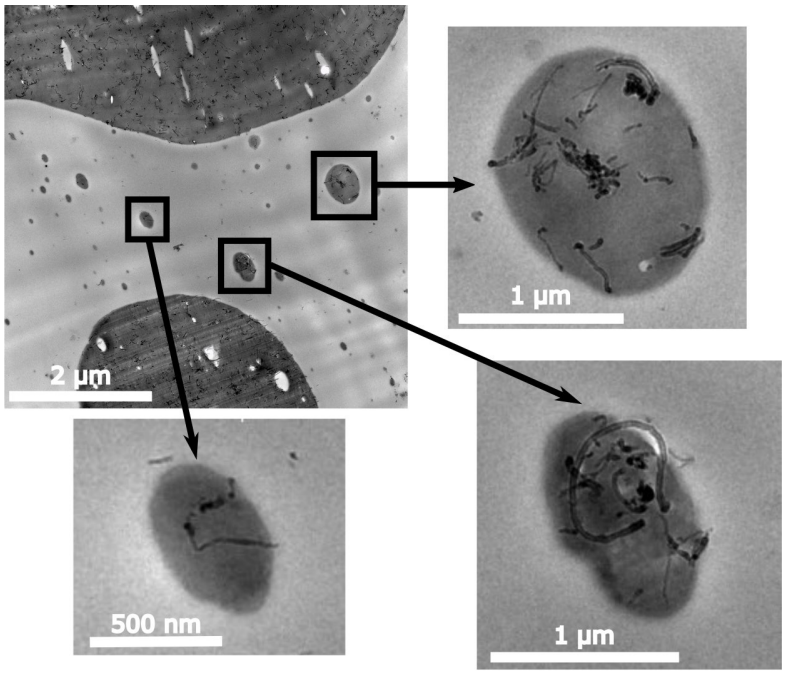

Figure 2.5: TEM images of the 50/50 weight ratio PS2CNT/PLA blend, showing the extremely selective localiza-tion of MWCNTs in PS small inclusions in the PLA phase.

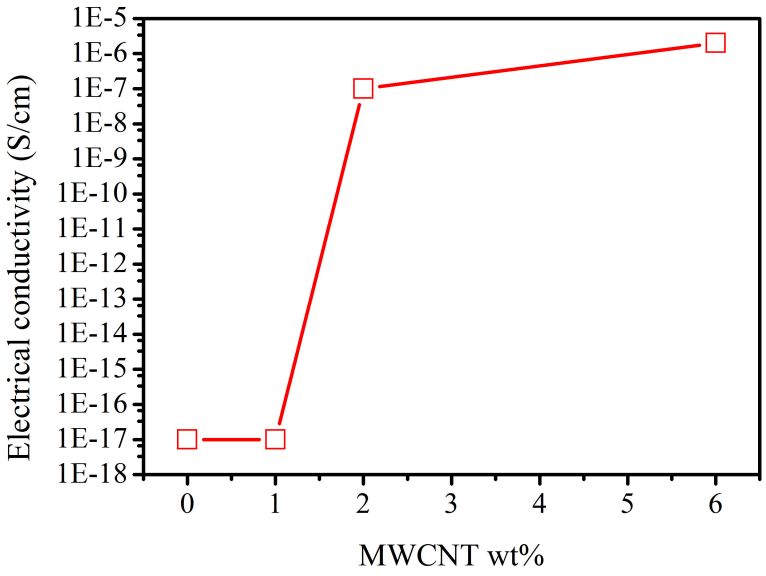

Figure 2.6: Electrical conductivity of PS/MWCNT composites as function of the MWCNT content.

Electrical conductivity

The electrical conductivity of the different PS masterbatches were compared in order to evaluate the minimum concentration of MWCNT needed to reach the electrical percolation threshold. As it can be seen in Figure 2.6, the 1 wt% MWCNT masterbatch does not show any electrical conductivity difference compared to pure PS (i.e. 10^17 S/cm). For the sample containing 2 wt% MWCNT the electrical con-ductivity was raised by 10 orders of magnitude (10^{-7} S/cm). The increase of MWCNT content to 6 wt% MWCNT further increased the conductivity of only one order of magnitude, indicating that the electrical percolation threshold was already reached at 2 wt%. For this reason we selected the masterbatch PS2CNT for the preparation of the blends with PLA at different PS2CNT/PLA weight ratios.

Figure 2.7(a) shows the electrical conductivity of the molded disks for the PS2CNT/PLA blends at different compositions. The red line indicates unchanged electrical conductivity values with respect to the unfilled PLA. In 2007 Pötschke et al. [65] showed that one explanation for the loss of electrical conductivity in a MWCNT/polymer blend can be related to the

destruction of the percolative network when the system is subjected to a transient shear. In this case a thermal annealing process can help to fully recover the electrical conductivity giving to the system enough thermal energy to reconstruct the MWCNT network. Another possible explanation is related to the morphological structure of the system. Zhang et al. [66] have shown that compression molding of a bicontinuous PS/PLA blend can result in the formation of a PLA insulating surface layer that can be reabsorbed in the bulk thanks to an annealing treatment. The formation of a superficial insulating layer was also found in the work of Gigli et al. [67] where a solvent cast film of MWCNT and polypropylene needed a plasma etching treatment to expose the nanoparticles, as they were covered by an insulating thin layer of polymer. On these bases, we performed a thermal post-treatment on the molded PS2CNT/PLA samples at different temperatures (120, 140, 160 and 180 °C) for 1 h, repeating the electrical conductivity tests after the annealing. The first sample, annealed at 120 °C showed no macroscopic deformation, but at the same time no recovery in electrical conductivity was noticed. The other three samples showed, conversely, a clear increase in electrical conductivity of several orders of magnitudes ($\sim 10^9$ S/cm) but different macroscopic appearances. The two samples annealed at higher temperatures (160 and 180 °C) were clearly deformed due to complete melting of the polymers and the bicontinuous morphology was lost, as proved by the samples breakdown after solvent extraction of PS. Only the sample annealed at 140 °C for 1 h showed both the electrical conductivity recover and a bicontinuous structural integrity. As both of the mechanisms described above, i.e. the reconstruction of the nanoparticle network and the reabsorption of an external insulating polymer layer, could be responsible for the recover in the electrical conductivity, we analyzed through TEM and SEM imaging both the nanotube dispersion state in the bulk and the surface morphology of solvent extracted samples. TEM analysis (Figure 2.8) showed no evidence of nanotube network reconstruction because the dispersion state of MWCNTs in the PS phase after annealing was comparable to that evaluated on thermally untreated samples. Instead, by comparing the surfaces of the PS2CNT/PLA 50/50 sample before and after annealing (Fig-

ure 2.7(a,b)), it is evident that the thermal treatment can effectively cause the partial re-absorption of the insulating PLA surface layer. This phenomenon was confirmed by temperature-controlled SEM experiments, in which during heating from room temperature to 140 °C, a progressive increase of contrast was recorded due to the absorption of the PLA layer and the progressive exposure of the PS phase (dark regions in Figure 2.7(d)) to the surface of the PS2CNT/PLA 50/50 sample.

Once the annealing conditions were optimized, the electrical conductivity was measured on samples with different PS2CNT/PLA weight ratios. As shown by the blue line in Figure 2.7(e), after the annealing all the samples above 40 wt% of PS2CNT showed an increase of the electrical conductivity of more than 8 orders of magnitude (from 10^{-17} to 10^{-9} S/cm). It is worth to be noted that the total amount of MWCNT for the 40 wt% PS2CNT sample is 0.8 wt%, leading to a MWCNT percent content of about 0.45 vol% on total volume (using 2.1 g/cm^3 density for MWCNT [68], 1.25 g/cm^3 for PLA and 1.05 g/cm^3 for PS). The final electrical conductivity obtained for PS2CNT/PLA blends is 2 orders of magnitude lower than the value showed by the PS2CNT masterbatch. Similar results were obtained by Pötschke et al. [34] and Fina et al. [69], and can be explained by considering the reduced amount of electrically conductive material (in our case the PS2CNT phase), as well as the longer electrically conductive path due to the bicontinuous structure. According to this hypothesis, electrons are forced to follow a much longer pathway to go from one side to the other side of the sample, because they must follow the percolative MWCNT network within the tortuous PS phase that percolates the complete volume of the sample.

2.2.5 Conclusions

In this work we reported the preparation of double percolated blends of PS, PLA and MWCNT starting from a PS masterbatch containing 2 wt% MWCNT. Melt mixing of the PS masterbatch and PLA, under proper process conditions, led to a double percolated morphology. The blends showed bicontinuity and, after a thermal annealing post-treatment, an exponential elec-

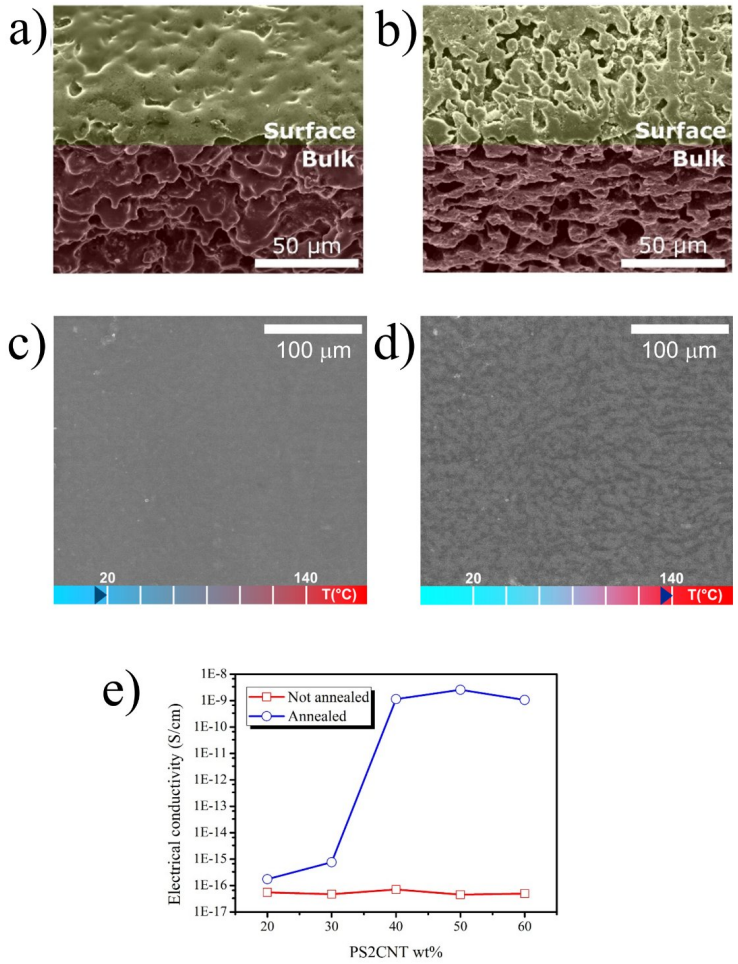

Figure 2.7: False color SEM images of extracted PS2CNT/PLA 50/50 before (a) and after (b) annealing, showing both surface and bulk of the samples; temperature-controlled SEM analysis of PS2CNT/PLA 50/50 before (c, 20 °C) and after (d, 140 °C) heating (see also movie S2 in the supporting information); electrical conductivity of PS2CNT/PLA blends as a function of the PS2CNT weight content before (blue line) and after (red line) annealing (e).

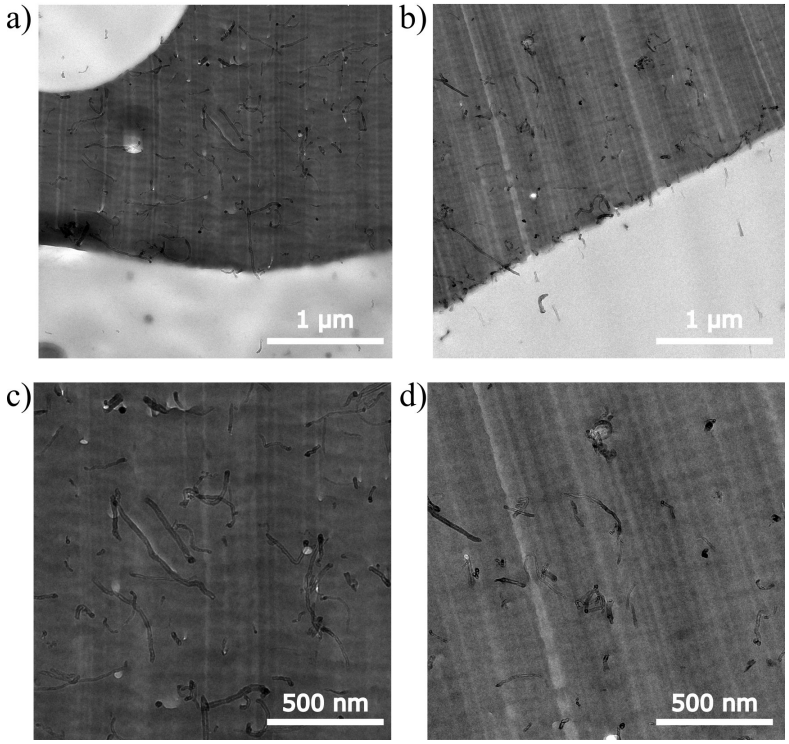

Figure 2.8: TEM images of MWCNTs dispersion state in PS2CNT/PLA samples before (a,c) and after (b,d) annealing.

trical conductivity increase of about 8 orders of magnitude. Therefore, the possibility of obtaining electrically conductive polymers by using MWCNT selectively dispersed in a multiphasic matrix was demonstrated. The blend micro-structuring had a key role in significantly reduce the electrical percolation threshold of the system, and in turn the total amount of nanoparticles needed to improve the electrical performance of the samples.

References

[1] Bernd Wetzel, Frank Haupert, and Ming Qiu Zhang. "Epoxy nanocomposites with high mechanical and tribological performance". In: *Composites Science and Technology* 63.14 (2003), pp. 2055–2067.

[2] D Qian et al. "Load transfer and deformation mechanisms in carbon nanotube-polystyrene composites". In: *Applied physics letters* 76.20 (2000), pp. 2868–2870.

[3] Mohammad Moniruzzaman and Karen I Winey. "Polymer nanocomposites containing carbon nanotubes". In: *Macromolecules* 39.16 (2006), pp. 5194–5205.

[4] Linda Vaisman, H Daniel Wagner, and Gad Marom. "The role of surfactants in dispersion of carbon nanotubes". In: *Advances in colloid and interface science* 128 (2006), pp. 37–46.

[5] Shimou Chen et al. "A new approach to the functionalization of single-walled carbon nanotubes with both alkyl and carboxyl groups". In: *Chemical Physics Letters* 402.4 (2005), pp. 312–317.

[6] T Ramanathan et al. "Amino-functionalized carbon nanotubes for binding to polymers and biological systems". In: *Chemistry of Materials* 17.6 (2005), pp. 1290–1295.

[7] Young Seak Lee et al. "Surface properties of fluorinated single-walled carbon nanotubes". In: *Journal of fluorine chemistry* 120.2 (2003), pp. 99–104.

[8] Ajay Garg and Susan B Sinnott. "Effect of chemical functionalization on the mechanical properties of carbon nanotubes". In: *Chemical Physics Letters* 295.4 (1998), pp. 273–278.

[9] Nanda Gopal Sahoo et al. "Polymer nanocomposites based on functionalized carbon nanotubes". In: *Progress in polymer science* 35.7 (2010), pp. 837–867.

[10] R Haggenmueller et al. “Aligned single-wall carbon nanotubes in composites by melt processing methods”. In: *Chemical physics letters* 330.3 (2000), pp. 219–225.

[11] Zdenko Spitalsky et al. “Carbon nanotube–polymer composites: chemistry, processing, mechanical and electrical properties”. In: *Progress in polymer science* 35.3 (2010), pp. 357–401.

[12] Ming Wen et al. “The electrical conductivity of carbon nanotube/carbon black/polypropylene composites prepared through multistage stretching extrusion”. In: *Polymer* 53.7 (2012), pp. 1602–1610.

[13] Rui M Novais et al. “The influence of carbon nanotube functionalization route on the efficiency of dispersion in polypropylene by twin-screw extrusion”. In: *Composites Part A: Applied Science and Manufacturing* 43.12 (2012), pp. 2189–2198.

[14] Yan Yan Huang and Eugene M Terentjev. “Dispersion of carbon nanotubes: mixing, sonication, stabilization, and composite properties”. In: *Polymers* 4.1 (2012), pp. 275–295.

[15] Harm Veenstra et al. “On the mechanical properties of co-continuous polymer blends: experimental and modelling”. In: *Polymer* 41.5 (2000), pp. 1817–1826.

[16] Cédric Calberg et al. “Electrical and dielectric properties of carbon black filled co-continuous two-phase polymer blends”. In: *Journal of Physics D: Applied Physics* 32.13 (1999), p. 1517.

[17] RC Willemse et al. “Co-continuous morphologies in polymer blends: a new model”. In: *Polymer* 39.24 (1998), pp. 5879–5887.

[18] LH Sperling and VBAT Mishra. “The current status of interpenetrating polymer networks”. In: *Polymers for Advanced Technologies* 7.4 (1996), pp. 197–208.

[19] Daniel Klempner, Leslie Howard Sperling, and Leszek A Utracki. *Interpenetrating polymer networks*. Tech. rep. American Chemical Society, Washington, DC (United States), 1994.

[20] J Lyngaae-Jørgensen and LA Utracki. “Dual phase continuity in polymer blends”. In: *Makromolekulare Chemie. Macromolecular Symposia*. Vol. 48. 1. Wiley Online Library. 1991, pp. 189–209.

[21] Petra Pötschke and DR Paul. “Formation of co-continuous structures in melt-mixed immiscible polymer blends”. In: *Journal of Macromolecular Science, Part C: Polymer Reviews* 43.1 (2003), pp. 87–141.

[22] Defeng Wu et al. “Selective localization of multiwalled carbon nanotubes in poly (ε-caprolactone)/polylactide blend”. In: *Biomacromolecules* 10.2 (2009), pp. 417–424.

[23] Masao Sumita et al. “Dispersion of fillers and the electrical conductivity of polymer blends filled with carbon black”. In: *Polymer bulletin* 25.2 (1991), pp. 265–271.

[24] Suprakas Sinha Ray and Mosto Bousmina. “Effect of organic modification on the compatibilization efficiency of clay in an immiscible polymer blend”. In: *Macromolecular Rapid Communications* 26.20 (2005), pp. 1639–1646.

[25] Defeng Wu et al. “Selective localization of nanofillers: effect on morphology and crystallization of PLA/PCL blends”. In: *Macromolecular Chemistry and Physics* 212.6 (2011), pp. 613–626.

[26] Yongjin Li and Hiroshi Shimizu. “Novel morphologies of poly (phenylene oxide)(PPO)/polyamide 6 (PA6) blend nanocomposites”. In: *Polymer* 45.22 (2004), pp. 7381–7388.

[27] Florian Wode et al. “Selective localization of multi-wall carbon nanotubes in homopolymer blends and a diblock copolymer. Rheological orientation studies of the final nanocomposites”. In: *Polymer* 53.20 (2012), pp. 4438–4447.

[28] Andreas Göldel, Gaurav Kasaliwal, and Petra Pötschke. “Selective Localization and Migration of Multiwalled Carbon Nanotubes in Blends of Polycarbonate and Poly (styrene-acrylonitrile)”. In: *Macromolecular rapid communications* 30.6 (2009), pp. 423–429.

[29] BD Favis. “Factors influencing the morphology of immiscible polymer blends in melt processing”. In: *Polymer blends* 1 (2000), pp. 501–537.

[30] M Hara and JA Sauer. “Synergism in mechanical properties of polymer/polymer blends”. In: (1998).

[31] Leszek A Utracki. *Commercial polymer blends*. Springer Science & Business Media, 2013.

[32] Jørgen Lyngaae-Jørgensen et al. “Flow induced deformation of dual-phase continuity in polymer blends and alloys. Part I”. In: *Polymer Engineering & Science* 39.6 (1999), pp. 1060–1071.

[33] Frederic Gubbels et al. “Kinetic and thermodynamic control of the selective localization of carbon black at the interface of immiscible polymer blends”. In: *Chemistry of materials* 10.5 (1998), pp. 1227–1235.

[34] Petra Pötschke, Arup R Bhattacharyya, and Andreas Janke. "Morphology and electrical resistivity of melt mixed blends of polyethylene and carbon nanotube filled polycarbonate". In: *Polymer* 44.26 (2003), pp. 8061–8069.

[35] Xiaodong Zhao et al. "Tuning the dielectric properties of polystyrene/poly (vinylidene fluoride) blends by selectively localizing carbon black nanoparticles". In: *The Journal of Physical Chemistry B* 117.8 (2013), pp. 2505–2515.

[36] Giovanni Filippone et al. "Assembly of plate-like nanoparticles in immiscible polymer blends–effect of the presence of a preferred liquid–liquid interface". In: *Soft matter* 10.18 (2014), pp. 3183–3191.

[37] Teri Wang Odom et al. "Atomic structure and electronic properties of single-walled carbon nanotubes". In: *Nature* 391.6662 (1998), pp. 62–64.

[38] MM JEBBESSEN Treacy, TW Ebbesen, and JM Gibson. "Exceptionally high Young's modulus observed for individual carbon nanotubes". In: (1996).

[39] Jing Li et al. "Correlations between percolation threshold, dispersion state, and aspect ratio of carbon nanotubes". In: *Advanced Functional Materials* 17.16 (2007), pp. 3207–3215.

[40] Gennaro Gentile et al. "Pros and cons of melt annealing on the properties of MWCNT/polypropylene composites". In: *Polymer Degradation and Stability* 110 (2014), pp. 56–64.

[41] Veronica Ambrogi et al. "Multiwalled carbon nanotubes functionalized with maleated poly (propylene) by a dry mechano-chemical process". In: *Polymer* 53.2 (2012), pp. 291–299.

[42] I Balberg. "Tunneling and nonuniversal conductivity in composite materials". In: *Physical Review Letters* 59.12 (1987), p. 1305.

[43] John G Simmons. "Generalized Thermal J-V Characteristic for the Electric Tunnel Effect". In: *Journal of Applied Physics* 35.9 (1964), pp. 2655–2658.

[44] M Foygel et al. "Theoretical and computational studies of carbon nanotube composites and suspensions: Electrical and thermal conductivity". In: *Physical Review B* 71.10 (2005), p. 104201.

[45] Siqi Xu et al. "The viability and limitations of percolation theory in modeling the electrical behavior of carbon nanotube–polymer composites". In: *Nanotechnology* 24.15 (2013), p. 155706.

[46] Isaac Balberg. "Recent developments in continuum percolation". In: *Philosophical Magazine Part B* 56.6 (1987), pp. 991–1003.

[47] J Sandler et al. "Development of a dispersion process for carbon nanotubes in an epoxy matrix and the resulting electrical properties". In: *Polymer* 40.21 (1999), pp. 5967–5971.

[48] JKW Sandler et al. "Ultra-low electrical percolation threshold in carbon-nanotube-epoxy composites". In: *Polymer* 44.19 (2003), pp. 5893–5899.

[49] Rodney Andrews et al. "Fabrication of carbon multiwall nanotube/polymer composites by shear mixing". In: *Macromolecular Materials and Engineering* 287.6 (2002), pp. 395–403.

[50] Wolfgang Bauhofer and Josef Z Kovacs. "A review and analysis of electrical percolation in carbon nanotube polymer composites". In: *Composites Science and Technology* 69.10 (2009), pp. 1486–1498.

[51] Scott Kirkpatrick. "Percolation and conduction". In: *Reviews of modern physics* 45.4 (1973), p. 574.

[52] I Balberg and N Binenbaum. "Computer study of the percolation threshold in a two-dimensional anisotropic system of conducting sticks". In: *Physical Review B* 28.7 (1983), p. 3799.

[53] Souheng Wu. *Polymer interface and adhesion*. M. Dekker, 1982.

[54] Anne-Christine Baudouin, Christian Bailly, and Jacques Devaux. "Interface localization of carbon nanotubes in blends of two copolymers". In: *Polymer Degradation and Stability* 95.3 (2010), pp. 389–398.

[55] Petra Pötschke et al. "A novel strategy to incorporate carbon nanotubes into thermoplastic matrices". In: *Macromolecular Rapid Communications* 29.3 (2008), pp. 244–251.

[56] Jinrui Huang et al. "Control of carbon nanotubes at the interface of a co-continuous immiscible polymer blend to fabricate conductive composites with ultralow percolation thresholds". In: *Carbon* 73 (2014), pp. 267–274.

[57] Sharika Thankappan Nair et al. "Selective localisation of multi walled carbon nanotubes in polypropylene/natural rubber blends to reduce the percolation threshold". In: *Composites Science and Technology* 116 (2015), pp. 9–17.

[58] Cui Mao, Yutian Zhu, and Wei Jiang. "Design of electrical conductive composites: Tuning the morphology to improve the electrical properties of graphene filled immiscible polymer blends". In: *ACS applied materials & interfaces* 4.10 (2012), pp. 5281–5286.

[59] Arun K Kota et al. “Electrical and rheological percolation in polystyrene/MWCNT nanocomposites”. In: *Macromolecules* 40.20 (2007), pp. 7400–7406.

[60] Souheng Wu. “Formation of dispersed phase in incompatible polymer blends: Interfacial and rheological effects”. In: *Polymer Engineering & Science* 27.5 (1987), pp. 335–343.

[61] Girma Biresaw and CJ Carriere. “Interfacial tension of poly (lactic acid)/polystyrene blends”. In: *Journal of Polymer Science Part B: Polymer Physics* 40.19 (2002), pp. 2248–2258.

[62] V Khoshkava and MR Kamal. “Effect of surface energy on dispersion and mechanical properties of polymer/nanocrystalline cellulose nanocomposites”. In: *Biomacromolecules* 14.9 (2013), pp. 3155–3163.

[63] Souheng Wu. “Surface and interfacial tensions of polymer melts. II. Poly (methyl methacrylate), poly (n-butyl methacrylate), and polystyrene”. In: *The Journal of Physical Chemistry* 74.3 (1970), pp. 632–638.

[64] S Nuriel et al. “Direct measurement of multiwall nanotube surface tension”. In: *Chemical Physics Letters* 404.4 (2005), pp. 263–266.

[65] I Alig et al. “Electrical conductivity recovery in carbon nanotube–polymer composites after transient shear”. In: *physica status solidi (b)* 244.11 (2007), pp. 4223–4226.

[66] Wei Zhang, Sarang Deodhar, and Donggang Yao. “Geometrical confining effects in compression molding of co-continuous polymer blends”. In: *Annals of biomedical engineering* 38.6 (2010), pp. 1954–1964.

[67] Francesco Malara et al. “Flexible carbon nanotube-based composite plates as efficient monolithic counter electrodes for dye solar cells”. In: *ACS applied materials & interfaces* 3.9 (2011), pp. 3625–3632.

[68] John H Lehman et al. “Evaluating the characteristics of multiwall carbon nanotubes”. In: *Carbon* 49.8 (2011), pp. 2581–2602.

[69] Alberto Fina et al. “Morphology and conduction properties of graphite-filled immiscible PVDF/PPgMA blends”. In: *Polymers for Advanced Technologies* 23.12 (2012), pp. 1572–1579.

Chapter 3

Patterning of perovskite-polymer films by wrinkling instabilities

3.1 Introduction

Lead halide perovskite overview

The continuous rise of energy demand of the modern society has lead to the intensive adoption of fossil fuels and induced the global warming that is strongly influencing the economy and politic of the entire world.[1] A fast transition to renewable energy source is becoming every day more urgent to promote a cleaner atmosphere and stop the climate changing. The total solar energy delivered by the Sun to the Earth each day could, in theory, satisfy the entire world energy demand for more than 20 years. For this reason great efforts have been made to find efficient and cheap materials that could collect at least part these energy in photovoltaic devices. Silicon based technologies represents the majority of the commercialized devices. Recently the thin films solar cells have become an interesting field of research do to the lower carbon footprint and the shorter energy payback.[2, 3]

One type of thin film solar cells that has attracted a lot of attention is based on hybrid organo-metal halide perovskite. The outstanding performances of such material as solar light harvester and ambipolar conductor has lead in only few years to an astonishing 22.1% of efficiency[4], overcoming

other kind of cells that have been studied for more than 20 years.[2] Perovskite materials used in photovoltaic are based on methylammonium lead halide and lead halide salts where the halides species can be iodide, bromide or cloride adopting the ABX3 perovskite structure. This structure is formed by BX_6 octahedral sharing corners, where the B atom is the metal cation and X is one of the halides. The A cation is the usually the methylammonium but it can be any ion that will balance the charge and that can fit in cuboctahedral cavities. Recent studies have indicated that mixed-halide organic–inorganic hybrid perovskites can display electron–hole diffusion lengths of over 1 μm Depending on the stoichiometry of the halide content the material can significantly change its properties. In general the perovskite is used between a mesoporous TiO_2 or Al_2O_3 thin film and an organic polymer as hole conductors. Due to the high efficiency of such cells they have been considered for a possible use in commercial devices. They have properties similar to bulk inorganic semiconductors but can be processed at low temperatures using inexpensive and abundant materials. The main problem remains to be both the presence of lead in the perovskite (also if in a very small amount) and the very high prices of the organic hole conductor layers. For example the most adopted one is the (2,2',7,7'-tetrakis(N,N-di-p-methoxyphenylamine) 9,9'-spirobifluorene) with a current commercial cost over ten times that of gold and platinum. For the first problem some researches have focused on the possibility of substituting the lead with a much less polluting metal as the Sn[5] while other studies have been conducting in the finding of a different hole conducting layer[6].

Another very interesting application of hybrid organic-inorganic perovskite materials is in organic-inorganic light-emitting device (OILED) devices where it behave as the emitting layer. The efficiency values of these devices is promising and some works are still trying to understand the role of the inorganic component because in these devices the emission arises from the organic layer of the structure.[7] Moreover the possibility of change the organic cation is another important parameter in order to improve the luminescence efficiency and the emission color.

The outstanding performances of lead halide perovskites in photovoltaic

are related to the long carrier lifetimes and the low non-radiative recombination rates. As these properties are important also for the materials used for laser applications the perovskite has been adopted also in this field In 2015 Zhu *et Al* developed a wavelenght-tunable laser working at room-temperature based on a single crystal of lead halide perovskite.[8] The lasing threshold was found to be very low (220 nJ/c^2m and an interesting quality factor (~ 3600). They performed a kinetic analysis based on time-resolved fluorescence revealing a lasing quantum yield approaching the 100% thanks to a very little charge carrier trapping in these single-crystal nanowires. Moreover the emission colour could be easily tuned changing the halide stoichiometry of the crystals. All these properties makes perovskites ideal materials also for nanophotonics.

A very attractive idea for photovoltaic is the development of building integrated solar cells in order to maximize the surface area used for the harvesting of the solar light. Actually the majority of the photovoltaic devices are placed on the top of the roof of buildings. If the solar cells could be adopted to cover the entire façade of a building much more electrical power would be produced. This is obviously a trade-off between the necessity of harvest the solar light and the necessity of transparency for design and aesthetic reasons. Moreover they should have a neutral-color, with the possibility of change it when needed, in order to permit their adoption without restrictions. Also in this case the perovskite could be a solid choice. When silicon based solar cells have been used to obtain building integrated devices the only possible approach was to reduce its thickness. However due to the nature of the density of states of the crystalline semiconductor conduction and valence bands, the color of the cell assume red or brown tint depending on its thickness. It is worth to be noted that the same problem of a reddish/brownish colour would arise also for perovskite solar cells if the same strategy of a mere reduction of thickness would be adopted. In 2013 Eperon *et Al* [9] controlling the many parameters of the perovskite deposition managed to obtain a precise control of the final morphological microstructure. As perovskite films are deposited from a precursor solution spin-coatined on flat substrate, it typically contains many pores and microsctructures formed to minimize the

surface energy. Controlling the initial film thickness, annealing temperature, atmosphere, and solvent vapor pressure they could obtain the control of the coverage of surface of the substrate. The incomplete, but controlled, coverage of the device permitted lead to the formation of micrometrical islands of perovskite. Every single island absorbed the entire range of visible light meanwhile the almost uncovered part let the light pass through. Thank to this peculiar morphology the cell could still continue to produce electricity but showing a neutral-colored semi-transparency.

Perovskite has also been used in combination with polymers also if the production of nanocomposite containing it has been in very few cases. In 2015 Masi *et Al* demonstrated that a nanocoposite of Poly[2-methoxy-5-(2-ethylhexyloxy)-1,4-phenylenevinylene] (MEH-PPV) and methyl ammonium lead iodide can act as an active layer in optoelectronic devices fabricating a bulk hetero junction solar cell with an efficiency of 3%. This work showed the first successful replacement of fullerene species with MAPbI3 perovskite in a polymeric solar cell.[10]

Wrinkles overview

In opto-electronic devices the introduction of periodic structures has become a popular strategy to enhance the harvesting of the solar light. Many different kind of structures have been produced like strips, wires, pyramids or arrays of lenses in order to improve the quantity of light absorbed by the devices and increase the overall efficiency.[11, 12] On the other side wrinkles and folds are self-organizing structures arising from linear and nonlinear elastic instabilities, and can be easily formed over large areas.[13, 14, 15] Buckling and wrinkling are generally watched as problem in polymer thin film processing. On the other side researchers have always been fascinated by those phenomena and tried to control them. The development of techniques for the formation of controlled patterning has increased the interest in developing method to emulate and control the emerging patterns of wrinkles. Many applications have been developed from these studies starting from building cell templates, nanochannels for protein condensation, smart adhesives and

optical grating devices. [16, 17, 18, 19]

The most common method to produce wrinkles is based on the sequential deposition of thin films. The difference of the stiffness of the two films is the cause of wrinkles formation when any kind of mechanical strain is induced in the system, causing the instability and wrinkling. The wrinkle wavelength is usually a function of the thickness of the system and the relative stiffness of the substrate and the thin film.[15, 20] The amplitude of the wrinkles depends on the applied stresses and the magnitude of the induced strain mismatch.[20, 21, 22]

Many works have been conduct on the formation of wrinkles on different kind of materials. In 1998 Bowden *et Al* deposited a metal thin film on the surface of a thermally expanded polydimethylsiloxane (PDMS). [15] After cooling down the different retraction of the two films produced wrinkles with a wavelength of $20 - 50$ μm. They could control and orient the wrinkling direction using relief structures on the top of the PDMS substrate. Similarly in 2000 Huch *et Al* deposited a gold film on the surface of a photochemically patterned PDMS leading to different stiffness and thermal expansion coefficient.[23] The gold thin film was deposited on the warm PDMS and the compressive stress due to the cooling lead to the formation of wrinkles. A way to control the width (wavelength) of wrinkles was showed by Watanabe *et Al* in 2004 using a polypyrrole film and a polyurethane elastic sheet.[24] To obtain the pattern they started drewing the polyurethane sheet, then onto the sheet the polypyrrole film was formed while the substrate was kept drawn. In this way after the release of the polyurethane sheet wrinkles were obtained. This process allowed to control the thickness of the instabilities ranging from 5 to 100 μm , with a depth in the range 1-15 μm controlling the elongation ratio of the sheet. Self-assembled microstructures were realized by Yoo *et Al* in 2002 using a periodic pattern on an elastomeric mold that was placed on the surface of a bilayer metal-polymer film.[25] The instability was induced by heating the system above the glass-transition temperature of the polymer. Another interesting way of forming controllable nanowrinkles was showed by Fu *et Al* in 2009.[26] They deposited on a prestressed shape memory polystyrene sheet a metal and then, after activating the shape

memory effect, they obtained uniaxial aligned wrinkles.

Wrinkles have also been exploited in solar cell application by Kim *et Al* in 2012. They found that when wrinkles are compressed beyond one third of their wavelength form folds. They demonstrated that these folds effectively localize and trap light. When those folds were formed on the polymeric thin film of their organic solar cells a dramatical improvement of light harvesting was measured. The deep folding of the polymer acted as waveguides and showed plasmonic properties effectively redirecting the near-infrared light. The combination of all these behaviours lead to the increase of the cell photocurrent of 47%. Because the infrared light is usually minimally absorbed in flat surfaces devices the external quantum efficiency at the incident wavelenghts over 650 nm showed an astonishing increse of 600%.[27]

3.2 Article

3.2.1 Authors and affiliations

- Giuseppe Nasti[a,b]
- Sandy Sanchez[c]
- Ilja Gunkel[c]
- Sandor Balog[c]
- Baart Roose[c]
- Gennaro Gentile[b]
- Pierfrancesco Cerruti[b]
- Veronica Ambrogi[a]
- Cosimo Carfagna[b]
- Ullrich Steiner[c]
- Antonio Abate[c,*]

[a] Department of Chemical, Materials and Production Engineering, University of Naples "Federico II", Piazzale Tecchio 80, 80125 Napoli, Italy.

[b] Institute for Polymers, Composites and Biomaterials (IPCB-CNR), via Campi Flegrei 34, 80078 Pozzuoli (Na), Italy.

[c] Adolphe Merkle Institute, University of Fribourg, Chemin des Verdiers 4, CH-1700 Fribourg, Switzerland.

* Corresponding author

3.2.2 Abstract

Organic-inorganic perovskites are semiconductors materials used for optoelectronics and photovoltaics devices. Micron and submicron perovskite patterns have been explored in semitransparent photovoltaic and lasing applications. In this work we show that a polymeric media can be used to create perovskite patterning, in a novel and inexpensive method.

3.2.3 Results and discussion

Organic-inorganic perovskites are crystalline materials with the general formula ABX_3, where A is an organic cation, B is a divalent metal and X is a halide anion. The metal cations coordinate 6 halide ions in an octahedral shape and the organic ions are located in cuboctahedral cavities coordinating 12 halide ions within the crystal lattice. [28] They have been employed as crystalline semiconductors with high optical density, [29] excitonic behavior [30] and long-range ambipolar charge transport [31]. Compared to traditional inorganic semiconductors, organic-inorganic perovskites are made of abundant, low-cost starting compounds. They are solution processable and thus compatible with fast and inexpensive production techniques. Since the first pioneering studies of Mitzi in the 90s, [32] organic-inorganic perovskites have been used in a number of optoelectronic applications such as photovoltaics, [33, 34] photodetectors, [35] light emitting diodes, [36] transistors [37] and memory devices [38]. Their application in solar cells is most impressive, allowing the creation of solution processed devices with power conversion efficiencies that rival those of established inorganic technologies, only a few years after a first demonstration by Miyasaka et al. in 2009. [39, 40] Furthermore, Eperon, et al. [9] demonstrated the possibility of manufacturing semitransparent perovskite solar cells, which are particularly desired for building integration. Compared to other semi-transparent photovoltaic devices, they are highly color- neutral. Transparency is achieved by means of dewetting of the perovskite absorbing layer, resulting in the spontaneous formation of discrete micron-sized perovskite domains during the sample preparation process. In contrast, uniform perovskite deposition was enhanced by adding a small amount of Poly(2-ethyl-2-oxazoline) (PEOXA) to the precursor solution. [41] More recently, patterning of perovskites on submicron length scales was explored for the preparation of optical cavities to enhance the light amplification in light-emitting and laser diodes. [42] Cheng et al. showed that luminescent patterned perovskite films can be obtained using soft lithography. [43] Sutherland et al. also demonstrated the possibility of achieving coherent light emission by deposition of a thin perovskite layer into

a spherical optical cavity. [44] More recently, Alias et al. [45] reported a new patterning procedure based on a focused-ion beam to pattern perovskites on micron and submicron length scale for photonic devices. While these successful applications demonstrated the enormous potential of patterned perovskite films, most of these approaches involve several processing steps and, more importantly, are not scalable.

In this work, we introduce a novel approach for patterning perovskite crystals on a flat substrate. The novelty relies on the exploitation of a polymeric media as perovskite nanocrystals carrier. Many different methods of polymers patterning available in literature could be used to obtain the desired pattern. Here we use a long-range uniform patterning is then induced by spontaneous wrinkling of the perovskite-polymer film in an oxygen plasma. The perovskite nanocrystals concentrate within the wrinkles, transferring the polymer pattern to a perovskite assembly. Atomic force microscopy and dynamic light scattering were employed to show that the dimensions of the wrinkles and the perovskite crystals can be tuned simply by controlling the thickness of the polymer film and the perovskite precursors concentration.

Wrinkling of thin films via an instability under compressive stresses leads to the micron and submicron patterning of polymers. [46, 47] A facile way to obtain such a system is to fabricate films having two or more layers with different elastic moduli. The relaxation of a compressive stress, uniaxially (i.e. by releasing an external load) or isotropically (i.e. contraction after thermal expansion or swelling), leads to spontaneous wrinkling of the stiffer layer to lower the total energy of the system. Evensen et al. demonstrated that it is possible to achieve controlled wrinkle patterns in argon plasma treated thin films of polydimethylsiloxane (PDMS). Here, the Ar plasma fulfilled two functions, 1) it crosslinked the PDMS film and 2) it formed a thin silica surface layer with a higher elastic modulus than that of the remaining polymer. [48] Recently, Lee et al. pointed out that controlled wrinkling of a polystyrene (PS) thin film caused by consecutive plasma exposures created three-dimensional hierarchical patterns. [49] A similar result can be achieved by creating a crosslinking gradient across the thin polymer layer, as shown by Guvendiren et al., who exploited the quenching of radicals from atmospheric

O_2 during UV curing of a thin poly(hydroxyethyl methacrylate) (PHEMA) layer, employing ethylene glycol dimethacrylate, (EGDMA) as cross-linker and a photoinitiator. [50]

Here, the formation of wrinkles in thin polyethylene glycol diacrylate (PEGDA) films was induced by a crosslinking gradient that formed during an O_2 plasma treatment. Thin PEGDA films were prepared by spin coating PEGDA/toluene solutions, with polymer concentrations ranging from 5% to 25% (v/v), onto glass substrates with or without a conductive layer of fluorine tin oxide (FTO). The film thickness was controlled by adjusting the concentration of PEGDA in toluene and the spin coating speed in the range of 2000 rpm to 8000 rpm. The as spun liquid PEGDA (Mn = 700 g/mol) films were immediately exposed to an O_2 plasma, which resulted in a change of the film appearance from transparent to whitish, caused by the increased light scattering from the wrinkles that have formed at the film surface. The formation of wrinkles was confirmed by optical microscopy in transmission, shown in Figure 3.1(a). The wrinkles were homogenously and isotropically distributed on the surface. The half-cylindrical shape of the wrinkles gives rise to a focusing of light onto the cylinder axis. The size and shape of the wrinkles were determined by scanning electron microscopy (SEM), shown in Figure 3.1(b). Note that the PEGDA film entirely covers the FTO substrate as confirmed by the absence of FTO crystals in the SEM image, which otherwise would be clearly visible (cf. Figure 3.2). The topography of the wrinkles was characterized by atomic force microscopy (AFM). Figure 3.1(c) shows a 3D AFM image of a wrinkled PEGDA thin film that had an as spun thickness of 1 µm before the O_2 plasma treatment. Both the width and height of the wrinkles are in the 1-3 µm range and confirms their nearly cylindrical shape. As shown in Figure 3.1(d) (and Figures 3.4 and 3.2.5) the wrinkle dimensions depend on the as-spun thickness of the PEGDA film and can be adjusted by varying the polymer solution concentration and the spinning speed during spin-coating. The variation of the wrinkle dimensions (Figure 3.1(d), blue line) on the initial PEGDA film thickness (Figure 3.1(d), red line) agrees with the Cerda and Mahadevan theory. [46]

Obtaining well-dispersed perovskite nanocrystals from PEGDA solutions

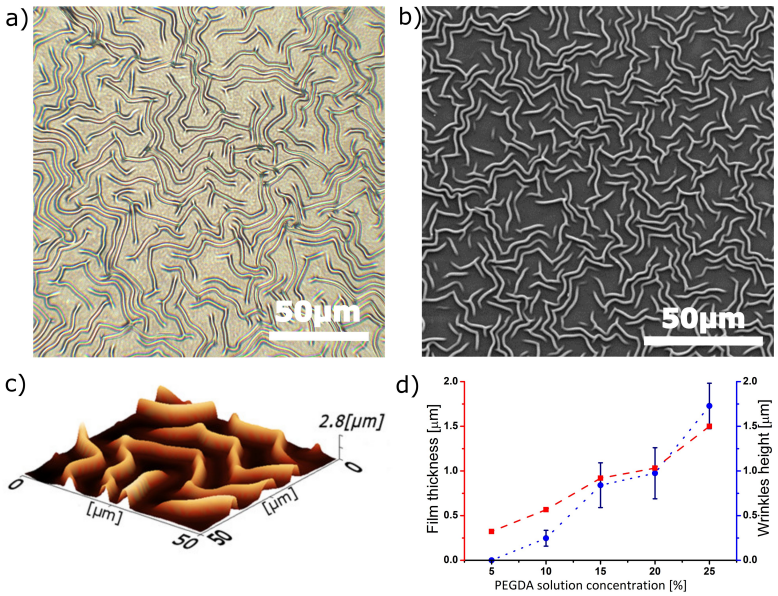

Figure 3.1: Optical microscopy (a) and SEM (b) images of wrinkled PEGDA layers deposited on FTO coated glass slides followed by an O_2 plasma treatment. (c) 3D AFM image of the wrinkle topography. (d) Variation of the PEGDA film thickness (before plasma curing, measured by ellipsometry) and wrinkle height (measured by AFM) with the solution concentration used to spin-coat the film, for a constant spin speed.

requires the precise control of the processing conditions. Pérez- Prieto et al. [51, 52] showed that highly luminescent and stable perovskite nanocrystals can be prepared from a dispersion in toluene stabilized by alkyl ammonium chains at the crystal surface. It is well known that the material bandgap can be tuned by changing the halide composition [53] or the temperature of the precipitation solvent. [54] One of the first attempts to embed a perovskite phase in a dielectric polymeric matrix can be found in the work by Li et al. [55] who produced light emitting diodes (LEDs) with a remarkably improved external quantum efficiency. In a similar way Masi et al. [10] embedded perovskite nanocrystals into a semiconducting polymer and manufactured a photovoltaic device with a power conversion efficiency (PCE) up to 3%.

Here, $CH_3NH_3PbBr_3$ perovskite nanocrystals were functionalized with octylammonium iodide (OAI) alkyl chains as a model perovskite material. The perovskite crystals were prepared from a precursor solution of methylammonium bromide (MABr), octyl ammonium iodide (OAI) and lead bromide ($PbBr_2$) in N,N-dimethylformamide (DMF). Three different 1.0 M solutions of MABr, OAI and $PbBr_2$ in DMF were prepared. MABr and PbBr2 solutions were mixed in 1:1 volume ratio for non-OAI-capped crystals leading to a 0.5 M solution of (OAI)$PbBr_2$. For capped crystals $PbBr_2$, MABr and OAI solutions were mixed with volume ratios of 10:9:1 resulting in a 0.5 M solution of $(MABr)_x(OAI)_{1-x}PbBr_2$ with x equal to 0.1. The 0.1 M and the 0.01 M were derived by dilution of the 0.5 M solution adding proper amount of DMF. Crystals were formed upon slow injection of one of the precursor solution in 2 mL of toluene under intense stirring. Each injection consisted in 5 μL of precursor for a total volume injected of 50 μL. The total volume of precursor solution was kept constant for the three cases (0.5 M, 0.1 M and 0.01 M) to reduce the influence of any residual DMF on dissolution and recrystallization during the spin coating process. The final volume ratio between DMF and toluene was 2.5% v/v. The solution color turned from transparent to orange immediately after the injection of the first drop, clearly indicating the formation of perovskite crystals. The need of the presence of OAI was evidenced by dispersion stability tests. Mixing MABr and $PbBr_2$ also led to the formation of an orange solution, but after a few minutes (less than 10

minutes) a precipitate was found on the bottom of the vial. After 24 hours the solution became clear, indicating that all the perovskite crystals precipitated to the bottom. In contrast, crystals formed in the presence of OAI were very stable and only a small fraction of the crystals precipitated after a week. The concentration of the precursor solution is another important control parameter for the formation of perovskite crystals. Three different concentrations were tested: 0.5 M, 0.1 M and 0.01 M. It was found that the concentration of the precursor solution affects both the crystal size and the dispersion stability, as demonstrated by dynamic light scattering (DLS).

SEM images of the perovskite crystals deposited by drop casting solutions at different concentrations on the top of a FTO glass slide are shown in Figure 3.2(a) (and 3.6). The substrate was quickly heated to 150 °C to avoid recrystallization caused by residual DMF. The formed crystals were almost perfectly cubic with sizes below 500 nm but with relatively high polydispersity. DLS measurements of the perovskite dispersions were performed to study the effect of precursor concentration on the average size of the crystals. As shown in Figure 3.2(b) a strong correlation between the average hydrodynamic size and the molarity of the precursor solution was found, ranging from 800 nm for a 0.5 M solution to 130 nm for 0.01 M (average size distribution in Figure 3.7). The formation of $CH_3NH_3PbBr_3$ crystals was also investigated by X-ray diffraction (XRD). Figure 3.2(c) shows narrow peaks that can be attributed to perovskite nanocrystals and FTO crystals on the substrate. [52, 56] The absorption spectra in the ultra violet (UV) and visible (Vis) wavelength range were measured. In Figure 3.2(d), the crystals obtained from the 0.5 M precursor solution give rise to an excitonic peak at 535 nm , as previously reported in literature. [30] This peak is clearly blue-shifted with decreasing average size of the particles. While this effect has been observed previously by Di et al., its origin is still debated. [57]

For the preparation of perovskite-polymer films, a toluene dispersion of perovskite crystals was mixed with PEGDA. It is important to emphasize that the OAI functionalization of perovskite crystals had not only the role of dispersion stabilization but also reduces the interaction between methylammonium cations and acrylic groups of the polymer. When PEGDA was

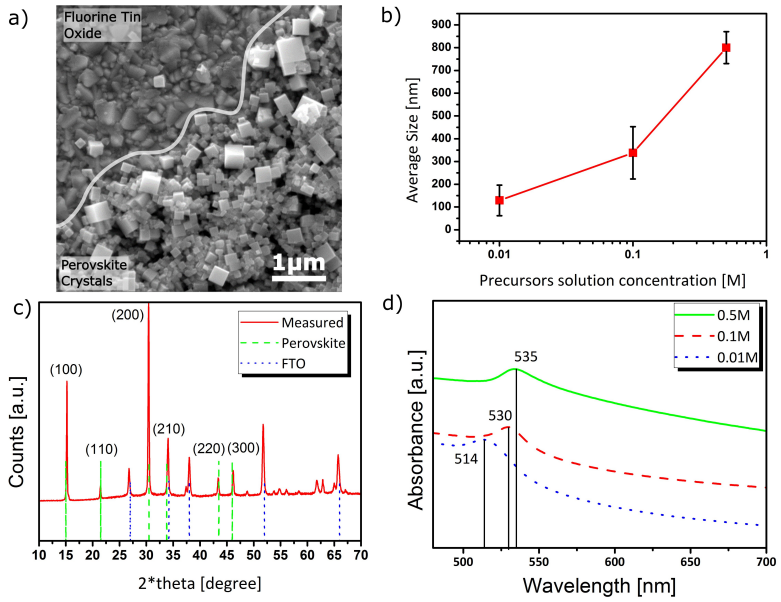

Figure 3.2: (a) SEM image of perovskite crystals that have formed on top of an FTO covered glass slide. (b) DLS measurement showing a reduction of average hydrodynamic crystal size with decreasing precursor solution concentration. (c) XRD measurement confirming the lattice structure of perovskite crystals. (d) UV-vis absorption spectra for crystals with different average size; a blue shift of excitonic peak is clearly visible and can be related to quantum confinement effects.

mixed with a toluene suspension of OAI-free perovskite crystals, the solution turned from orange to transparent within a few seconds. With OAI stabilized nanoparticles, no color change of the solution was observed. The mixed solutions of perovskite crystals and PEGDA in toluene were processed as described above for the case of pure PEGDA solutions to obtain wrinkle-patterned films. Optical micrographs of perovskite-polymer hybrid films after O_2 plasma treatment (Figure 3.3(a) and 3.8) confirm the presence of perovskite crystals inside the ridge-structure formed by the PEGDA wrinkles. This is further confirmed by microscopy in fluorescence mode under UV illumination, were the green emission of the perovskite crystals is only observed from the wrinkles.

The localization of the perovskite crystals within the wrinkle morphology follows the mechanism that has been reported by Yoo et al., [58] who demonstrated that most of the material composing the film, and thus perovskite crystals dispersed within the film, migrates to accumulate within the wrinkles. In Figure 3.3(b), transmittance and photoluminescence (PL) spectra of perovskite filled wrinkles film are shown. A step-like behavior in transmittance and a sharp emission peak are clearly visible at 535 nm

3.2.4 Conclusions

We introduce a novel approach to achieve patterned perovskite-polymer films. Perovskite nanocrystals dispersed in a polymer matrix were prepared by spin-coating a perovskite-polymer solution onto flat substrates. Micrometer patterning was induced by the spontaneous wrinkling of the perovskite-polymer film under an oxygen plasma. Perovskite nanocrystals were predominantly located inside the ridge-structure formed by the polymeric wrinkles which introduce a characteristic lateral length scale into the film. This approach is potentially compatible with many different polymeric matrices and patterning techniques and can therefore potentially be exploited in a number of optoelectronic and photovoltaic applications. In contrast to the commonly used top-down patterning techniques, this approach enables solution processing and thus is very fast and inexpensive.

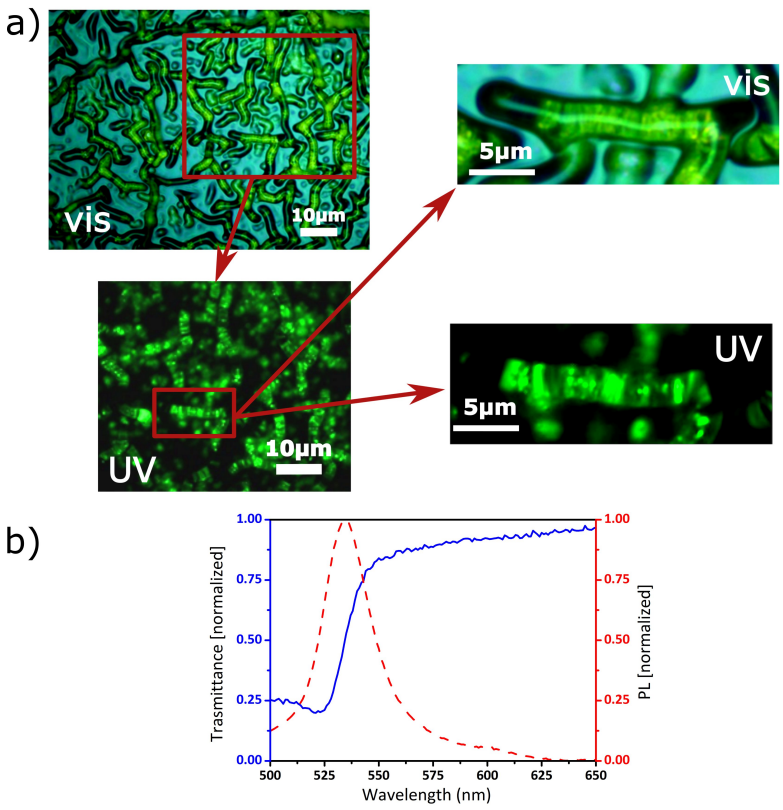

Figure 3.3: Light microscopy images of wrinkle patterns filled with perovskite crystals. (a, top) White light illumination; (a, bottom) UV illumination. The perovskite nanocrystals exhibit green fluorescence emission under UV light. Magnified images (a, right) evidence the efficient filling of wrinkles with nanoparticles. (b) Transmittance and emission spectra of perovskite crystals in the polymer. Green emission is clearly visible at 535 nm (dashed line) with the correspondent step-like absorbance transition (full line).

3.2.5 Supplementary

Materials

Fluorine doped tin oxide coated glass slides and all other chemicals were purchased from Sigma-Aldrich, excepted for methyl ammonium bromide purchased from TCI Deutschland Gmbh. All chemicals were used as purchased without further purification.

Methods

All experiments and measurements were performed at Adolphe Merkle Institute (AMI, Fribourg, Switzerland).

Thin films were prepared using a Laurell WS-400BZ spin coater.

Polymer crosslinking was performed in a Zepto Diener (40 kHz, 100 W max power) plasma etcher. After vacuum was formed into the chamber, pure oxygen was flushed into the chamber for 2 minutes in order to remove the residual N2. The plasma generator was then turned on for 30 seconds at 50 W, providing the radical species needed to crosslink PEGDA.

Wrinkles formation was checked using a Zeiss Axio Scope.A1 optical microscope in transmission mode.

Fluorescence microscopy was performed using an Olympus BX51 microscope equipped and an X-Cite (series 120Q) LED-light as UV source.

Scanning electron microscopy (SEM) images were obtained with a Tescan MIRA3 LM device.

JPK Instruments Nano Wizard II atomic force microscope (AFM) was used in intermittent contact mode (tapping) to topologically characterize wrinkles.

X-ray diffraction (XRD) measurements were performed using a Powder XRD Philips PW1800. The 2theta parameter was varied between 10° and 90° with a step size of 0.02°.

Dynamic light scattering (DLS) measurements were performed at 21 °C, with 90 °C detection, using a 3D LS Spectrometer (LS Instruments AG, Switzerland).

UV-vis spectra were acquired using a Specord 210 Plus (Analytik Jena) spectrofluorimeter using 1 cm quartz cuvettes.

The thickness of PEGDA thin films were measured with an alpha-SE Ellipsometer (J. A. Woollam Co., Inc., Lincoln, NE).

Photoluminescence measurements on perovskite filled films were performed using a Horiba Fluorolog FL 3-22 device.

Dynamic light scattering

Standard dynamic light scattering (DLS) data were collected at constant temperature (21 °C) at 90 deg., using a commercial goniometer instrument (3D LS Spectrometer, LS Instruments AG, Switzerland). The primary beam was formed by a linearly polarized and collimated laser beam (Cobolt 05-01 diode pumped solid state laser, $\lambda = 660$ nm , P max. $= 500$ mW), and the scattered light was collected by single-mode optical fibers equipped with integrated collimation optics. The collected light was coupled into two high-sensitivity APD detectors via laser- line filters (Perkin Elmer, Single Photon Counting Module), and their outputs were fed into a two-channel multiple-tau correlator. The signal-to-noise ratio was improved by cross-correlating these two channels. The corresponding field auto-correlation functions were obtained via the Siegert relation: $g_1(t) = \sqrt{g_2(t) - 1}$ where $g_2(t)$ is the intensity auto-correlation function constructed from the temporal fluctuations of the depolarized component of the scattered intensity.

For a dilute suspension of uniform spherical NPs of radius r, the correlation function is written as:

$$g_1(t) = e^{-\Gamma(q,r)t} \tag{3.1}$$

where

$$\Gamma(q, r) \equiv q^2 D_T \tag{3.2}$$

and

$$D_T = \frac{k_B T}{6\pi\eta} \frac{1}{r} \tag{3.3}$$

k_B is the Boltzmann constant, T the temperature, η the viscosity of the

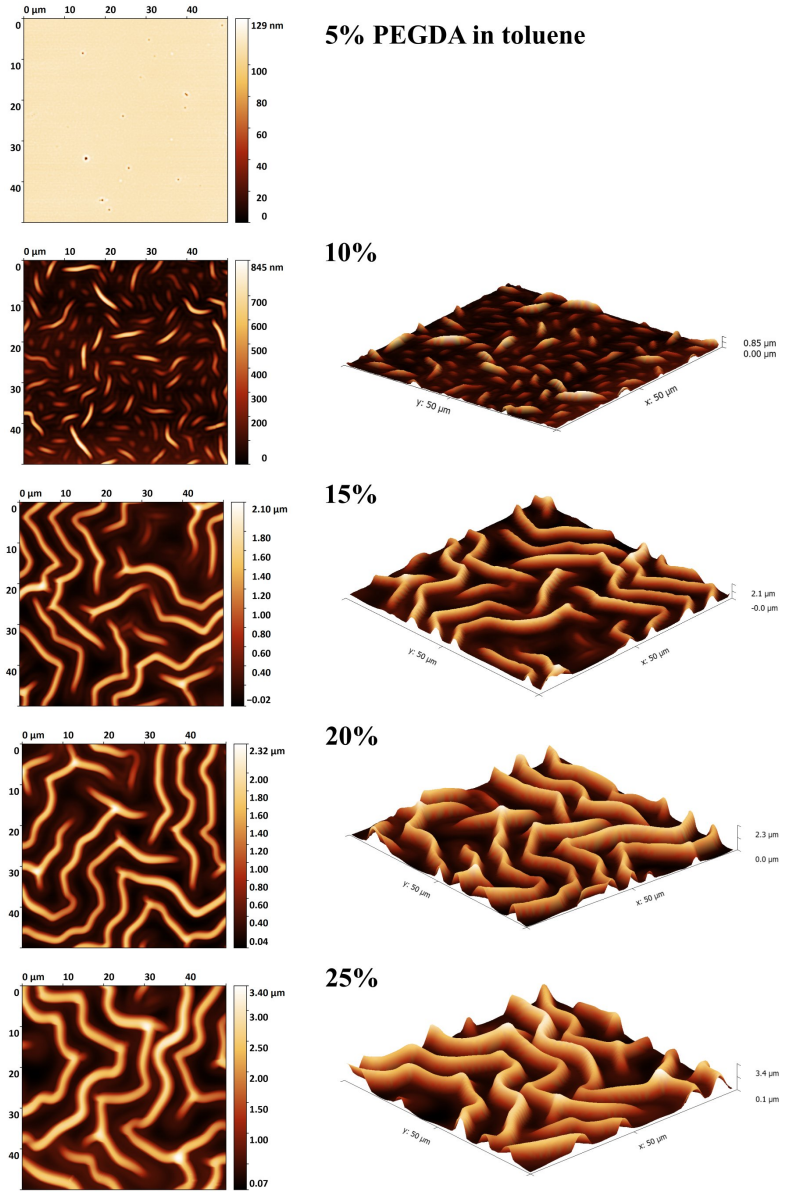

Figure 3.4: Atomic force microscopy (AFM) images of wrinkles on PEGDA films of different thickness after O_2 treatment. It is clearly noticed the dependence of wrinkles size in function of PEGDA/solvent volume ratio (i.e. film thickness, S4), at constant spin coating deposition speed (8000 RPM). For the lowest concentration (5%) no wrinkles formation was observed. From 10% to 25% wrinkles average height increases from 0.3 µm to 1.7 µm

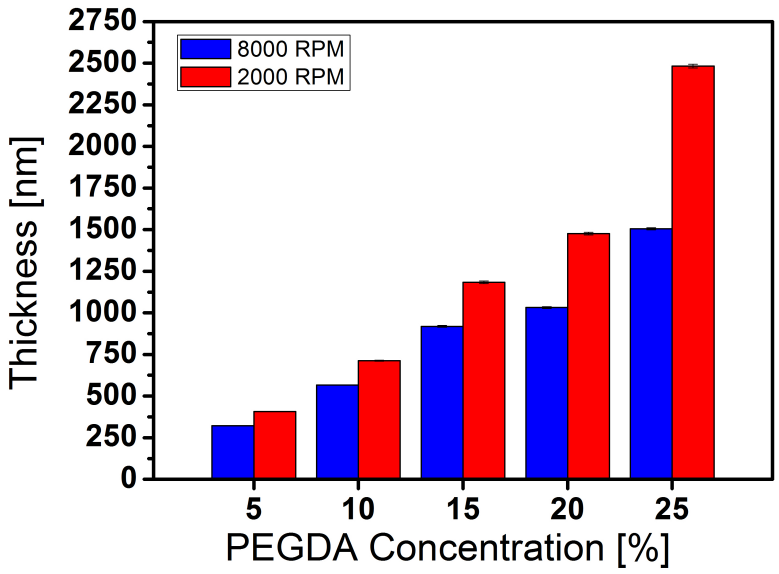

Figure 3.5: PEGDA thin films thickness measured through ellipsometry as a function of polymer concentration in toluene and spin coating deposition speed. It is clearly visible that is possible to control the polymer thickness by adjusting these two parameters.

solvent, q the momentum transfer $q = \frac{4\pi}{\lambda} n \sin\frac{\theta}{2}$, θ the scattering angle, λ the wavelength of the scattered waves, and n the refractive index of the solvent.

The field correlation function from polydisperse samples is frequently expressed as the Laplace transform of the probability density function describing the dispersion in the relaxation rate. Then the correlation function (Equation 3.1) is written as

$$g_1(t) = \int_0^{\inf} P(\Gamma) e^{-\Gamma t} d\Gamma \tag{3.4}$$

where $P(\Gamma)$ is the probability density function of the relaxation rates. $P(\Gamma)$ is modelled here by the (modified) Schulz–Zimm distribution:

$$P(\Gamma) = \frac{1}{\Gamma(\frac{1}{\sigma^2})} e^{-\frac{\Gamma}{\langle\Gamma\rangle\sigma^2}} \left(\frac{1}{\langle\Gamma\rangle\sigma^2}\right)^{\frac{1}{\sigma^2}} \Gamma^{\frac{1}{\sigma^2}-1} \tag{3.5}$$

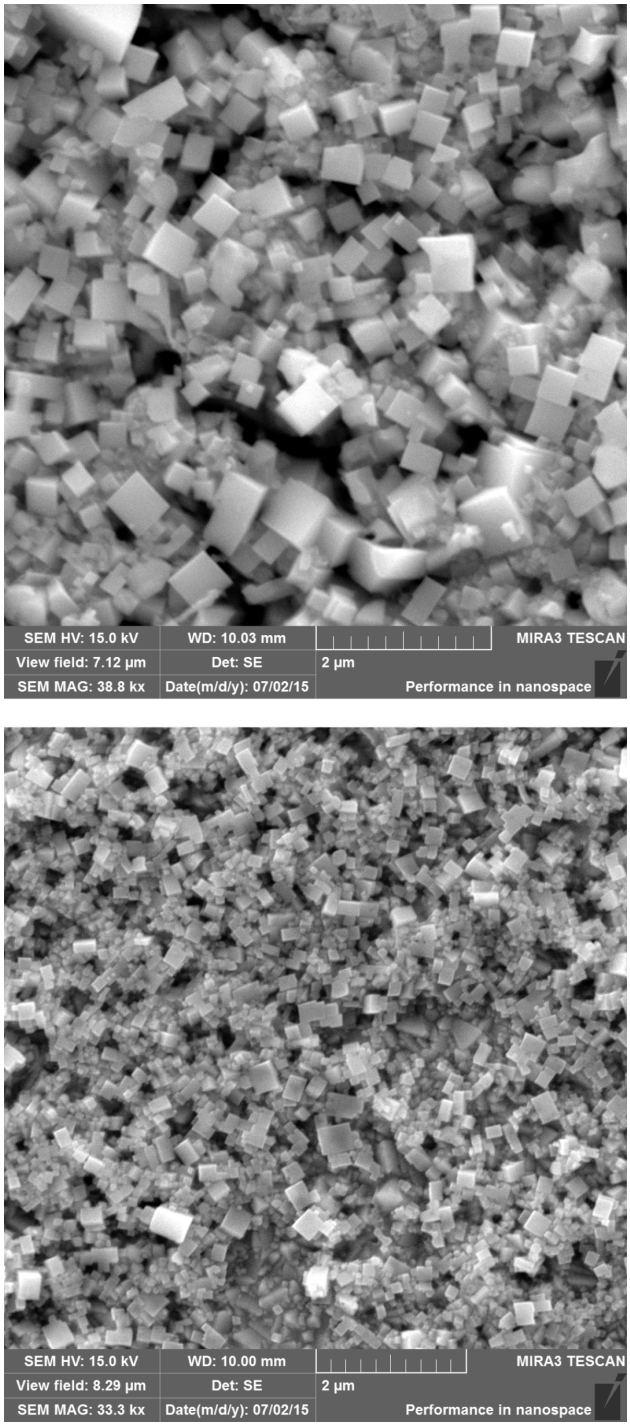

Figure 3.6: Scanning electron microscopy micrographs of perovskite nanocrystals synthesized starting from a 0.5M (top) and 0.01M (bottom) precursor solution.

where

$$\langle \Gamma \rangle = \int_0^{\inf} \Gamma P(\Gamma) d\Gamma \tag{3.6}$$

and

$$\sigma(\Gamma) \equiv \frac{\sqrt{var\Gamma}}{\langle \Gamma \rangle} \tag{3.7}$$

In case of a unimodal distribution $0 < \sigma \leq 1$. When σ is close to 1, the Schulz–Zimm distribution approaches an exponential distribution, and when σ is small, it approaches a Gaussian distribution. According to Equation 3.5, the correlation function is now written as

$$g_1(t) = (1 + \langle \Gamma \rangle \sigma^2 t)^{-\frac{1}{\sigma^2}} \tag{3.8}$$

The correlation functions and their respective best fit (Figure 3.7, Equation 3.8) corresponding to the three different concentrations of the perovskite precursor solution are shown below. The estimated apparent intensity-weighted average hydrodynamic were respectively 807 nm, 338 nm and 129 nm for 0.5M, 0.1M and 0.01M solutions. The intensity-weighted probability function of the hydrodynamic radius, $P_r(r)$, is estimated via applying the rule of transforming random variables. Let Φ represent the relationship between Γ and r (Equation 3.2 and 3.3). Then the probability density function of the intensity-weighted hydrodynamic radius is estimated via

$$P_r(r) = P_r(\Phi(r)) \cdot |\frac{d}{dr}\Phi(r)| \tag{3.9}$$

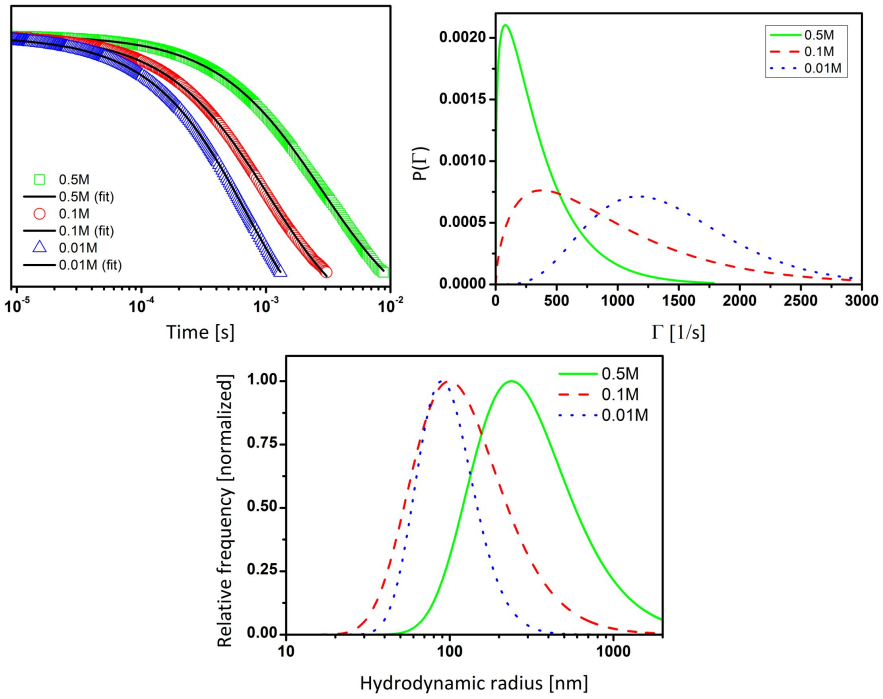

Figure 3.7: Correlation function and model fit (left) of the Equation 3.8 for 0.5M, 0.1M and 0.01M precursor solution concentrations (top left). Probability density function of the relaxation rates for the three samples (top right). Intensity-weighted probability density function of the hydrodynamic radius (bottom).

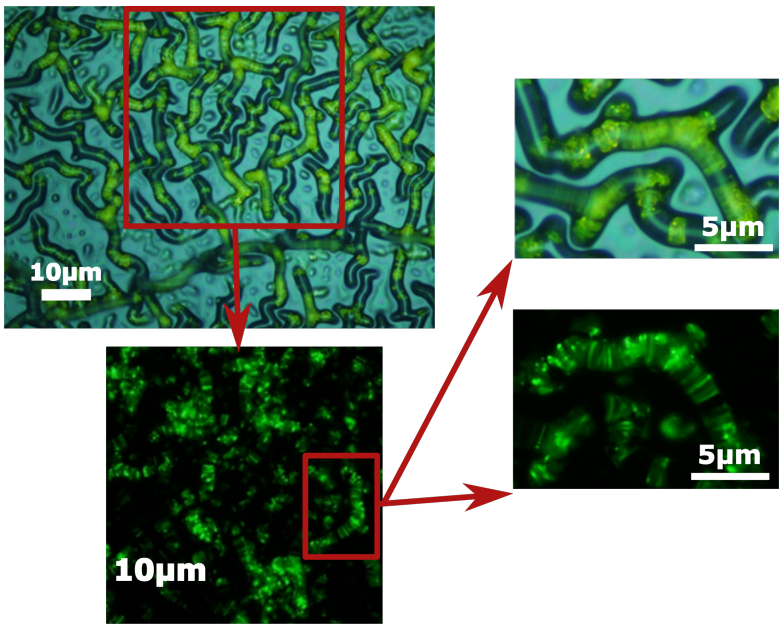

Figure 3.8: Wrinkles filled with perovskite crystals under visible light microscope (top) and under UV illumination (bottom). Perovskite nanocrystals green fluorescence emission is revealed under UV light. Magnifications is shown to prove the nice filling of the wrinkle with crystals.

References

[1] Klaus Desmet and Esteban Rossi-Hansberg. "On the spatial economic impact of global warming". In: *Journal of Urban Economics* 88 (2015), pp. 16–37.

[2] Gary Hodes. "Perovskite-based solar cells". In: *Science* 342.6156 (2013), pp. 317–318.

[3] Michael Dale and Sally M Benson. "Energy balance of the global photovoltaic (PV) industry-is the PV industry a net electricity producer?" In: *Environmental science & technology* 47.7 (2013), pp. 3482–3489.

[4] Silvia Collavini, Sebastian F Völker, and Juan Luis Delgado. "Understanding the Outstanding Power Conversion Efficiency of Perovskite-Based Solar Cells". In: *Angewandte Chemie International Edition* 54.34 (2015), pp. 9757–9759.

[5] Feng Hao et al. "Lead-free solid-state organic-inorganic halide perovskite solar cells". In: *Nature photonics* 8.6 (2014), pp. 489–494.

[6] Jeffrey A Christians, Raymond CM Fung, and Prashant V Kamat. "An inorganic hole conductor for organo-lead halide perovskite solar cells. Improved hole conductivity with copper iodide". In: *Journal of the American Chemical Society* 136.2 (2013), pp. 758–764.

[7] Konstantinos Chondroudis and David B Mitzi. "Electroluminescence from an organic-inorganic perovskite incorporating a quaterthiophene dye within lead halide perovskite layers". In: *Chemistry of materials* 11.11 (1999), pp. 3028–3030.

[8] Haiming Zhu et al. "Lead halide perovskite nanowire lasers with low lasing thresholds and high quality factors". In: *Nature materials* 14.6 (2015), pp. 636–642.

[9] Giles E Eperon et al. "Neutral color semitransparent microstructured perovskite solar cells". In: *ACS nano* 8.1 (2013), pp. 591–598.

[10] Sofia Masi et al. "Growing perovskite into polymers for easy-processable optoelectronic devices". In: *Scientific reports* 5 (2015).

[11] On Realizing Higher Efficiency Polymer Solar. "Cells Using a Textured Substrate Platform Nalwa, Kanwar S.; Park, Joong-Mok; Ho, Kai-Ming; Chaudhary, Sumit". In: *Advanced Materials (Weinheim, Germany)* 23.1 (2011), pp. 112–116.

[12] Kristofer Tvingstedt et al. "Trapping light with micro lenses in thin film organic photovoltaic cells". In: *Optics Express* 16.26 (2008), pp. 21608–21615.

[13] Pilnam Kim, Manouk Abkarian, and Howard A Stone. "Hierarchical folding of elastic membranes under biaxial compressive stress". In: *Nature materials* 10.12 (2011), pp. 952–957.

[14] Luka Pocivavsek et al. "Stress and fold localization in thin elastic membranes". In: *Science* 320.5878 (2008), pp. 912–916.

[15] Ned Bowden et al. "Spontaneous formation of ordered structures in thin films of metals supported on an elastomeric polymer". In: *Nature* 393.6681 (1998), pp. 146–149.

[16] Xingyu Jiang et al. "Controlling mammalian cell spreading and cytoskeletal arrangement with conveniently fabricated continuous wavy features on poly (dimethylsiloxane)". In: *Langmuir* 18.8 (2002), pp. 3273–3280.

[17] Edwin P Chan et al. "Surface wrinkles for smart adhesion". In: *Advanced Materials* 20.4 (2008), pp. 711–716.

[18] Christopher Harrison et al. "Sinusoidal phase grating created by a tunably buckled surface". In: *Applied Physics Letters* 85.18 (2004), pp. 4016–4018.

[19] Seok Chung et al. "Non-Lithographic Wrinkle Nanochannels for Protein Preconcentration". In: *Advanced materials* 20.16 (2008), pp. 3011–3016.

[20] Xi Chen and John W Hutchinson. "A family of herringbone patterns in thin films". In: *Scripta materialia* 50.6 (2004), pp. 797–801.

[21] Myoung-Woon Moon and Ashkan Vaziri. "Surface modification of polymers using a multi-step plasma treatment". In: *Scripta Materialia* 60.1 (2009), pp. 44–47.

[22] Sk Faruque Ahmed et al. "High aspect ratio wrinkles on a soft polymer". In: *Soft Matter* 6.22 (2010), pp. 5709–5714.

[23] Wilhelm TS Huck et al. "Ordering of spontaneously formed buckles on planar surfaces". In: *Langmuir* 16.7 (2000), pp. 3497–3501.

[24] Masashi Watanabe and Toshihiro Hirai. “Polypyrrole film with striped pattern”. In: *Journal of Polymer Science Part B: Polymer Physics* 42.13 (2004), pp. 2460–2466.

[25] Pil Jin Yoo et al. “Physical self-assembly of microstructures by anisotropic buckling”. In: *Advanced materials* 14.19 (2002), pp. 1383–1387.

[26] Chi-Cheng Fu et al. “Tunable nanowrinkles on shape memory polymer sheets”. In: *Advanced Materials* 21.44 (2009), pp. 4472–4476.

[27] Jong Bok Kim et al. “Wrinkles and deep folds as photonic structures in photovoltaics”. In: *Nature Photonics* 6.5 (2012), pp. 327–332.

[28] David B Mitzi. “Templating and structural engineering in organic–inorganic perovskites”. In: *Journal of the Chemical Society, Dalton Transactions* 1 (2001), pp. 1–12.

[29] Samuel D Stranks et al. “Electron-hole diffusion lengths exceeding 1 micrometer in an organometal trihalide perovskite absorber”. In: *Science* 342.6156 (2013), pp. 341–344.

[30] Valerio D’Innocenzo et al. “Excitons versus free charges in organo-lead tri-halide perovskites”. In: *Nature communications* 5 (2014).

[31] Yu-Che Hsiao et al. “Fundamental physics behind high-efficiency organo-metal halide perovskite solar cells”. In: *Journal of Materials Chemistry A* 3.30 (2015), pp. 15372–15385.

[32] David B Mitzi et al. “Conducting tin halides with a layered organic-based perovskite structure”. In: (1994).

[33] Nam Joong Jeon et al. “Compositional engineering of perovskite materials for high-performance solar cells”. In: *Nature* 517.7535 (2015), pp. 476–480.

[34] Akihiro Kojima et al. “Organometal halide perovskites as visible-light sensitizers for photovoltaic cells”. In: *Journal of the American Chemical Society* 131.17 (2009), pp. 6050–6051.

[35] Letian Dou et al. “Solution-processed hybrid perovskite photodetectors with high detectivity”. In: *Nature communications* 5 (2014).

[36] Zhi-Kuang Tan et al. “Bright light-emitting diodes based on organometal halide perovskite”. In: *Nature nanotechnology* 9.9 (2014), pp. 687–692.

[37] CR Kagan, DB Mitzi, and CD Dimitrakopoulos. “Organic-inorganic hybrid materials as semiconducting channels in thin-film field-effect transistors”. In: *Science* 286.5441 (1999), pp. 945–947.

[38] Zhengguo Xiao et al. “Giant switchable photovoltaic effect in organometal trihalide perovskite devices”. In: *Nature materials* 14.2 (2015), pp. 193–198.

[39] Woon Seok Yang et al. “High-performance photovoltaic perovskite layers fabricated through intramolecular exchange”. In: *Science* 348.6240 (2015), pp. 1234–1237.

[40] Martin A Green et al. “Solar cell efficiency tables (Version 45)”. In: *Progress in photovoltaics: research and applications* 23.1 (2015), pp. 1–9.

[41] Qifan Xue et al. “Metallohalide perovskite–polymer composite film for hybrid planar heterojunction solar cells”. In: *RSC Advances* 5.1 (2015), pp. 775–783.

[42] Guichuan Xing et al. “Low-temperature solution-processed wavelength-tunable perovskites for lasing”. In: *Nat. Mater* 13.5 (2014), pp. 476–480.

[43] ZY Cheng et al. “Patterning and photoluminescent properties of perovskite-type organic/inorganic hybrid luminescent films by soft lithography”. In: *Chemical physics letters* 376.3 (2003), pp. 481–486.

[44] Brandon R Sutherland et al. “Conformal organohalide perovskites enable lasing on spherical resonators”. In: *ACS nano* 8.10 (2014), pp. 10947–10952.

[45] Mohd Sharizal Alias et al. “Focused-ion beam patterning of organolead trihalide perovskite for subwavelength grating nanophotonic applications”. In: *Journal of Vacuum Science & Technology B* 33.5 (2015), p. 051207.

[46] Enrique Cerda and Lakshminarayanan Mahadevan. “Geometry and physics of wrinkling”. In: *Physical review letters* 90.7 (2003), p. 074302.

[47] Jenni E Koskela et al. “Light-Driven Surface Patterning of Supramolecular Polymers with Extremely Low Concentration of Photoactive Molecules”. In: *ACS Macro Letters* 3.11 (2014), pp. 1196–1200.

[48] HT Evensen et al. “Transformations in wrinkle patterns: cooperation between nanoscale cross-linked surface layers and the submicrometer bulk in wafer-spun, plasma-treated polydimethylsiloxane”. In: *Nano letters* 9.8 (2009), pp. 2884–2890.

[49] Won-Kyu Lee et al. “Controlled Three-Dimensional Hierarchical Structuring by Memory-Based, Sequential Wrinkling”. In: *Nano letters* 15.8 (2015), pp. 5624–5629.

[50] Murat Guvendiren, Shu Yang, and Jason A Burdick. "Swelling-Induced Surface Patterns in Hydrogels with Gradient Crosslinking Density". In: *Advanced Functional Materials* 19.19 (2009), pp. 3038–3045.

[51] Luciana C Schmidt et al. "Nontemplate synthesis of CH3NH3PbBr3 perovskite nanoparticles". In: *Journal of the American Chemical Society* 136.3 (2014), pp. 850–853.

[52] Soranyel Gonzalez-Carrero, Raquel E Galian, and Julia Pérez-Prieto. "Maximizing the emissive properties of CH 3 NH 3 PbBr 3 perovskite nanoparticles". In: *Journal of Materials Chemistry A* 3.17 (2015), pp. 9187–9193.

[53] Feng Zhang et al. "Brightly luminescent and color-tunable colloidal CH3NH3PbX3 (X= Br, I, Cl) quantum dots: potential alternatives for display technology". In: *ACS nano* 9.4 (2015), pp. 4533–4542.

[54] He Huang et al. "Control of Emission Color of High Quantum Yield CH3NH3PbBr3 Perovskite Quantum Dots by Precipitation Temperature". In: *Advanced Science* 2.9 (2015).

[55] Guangru Li et al. "Efficient light-emitting diodes based on nanocrystalline perovskite in a dielectric polymer matrix". In: *Nano letters* 15.4 (2015), pp. 2640–2644.

[56] Shao-Hui Hsu et al. "Platinum-free counter electrode comprised of metal-organic-framework (MOF)-derived cobalt sulfide nanoparticles for efficient dye-sensitized solar cells (DSSCs)". In: *Scientific reports* 4 (2014).

[57] Dawei Di et al. "Size-dependent photon emission from organometal halide perovskite nanocrystals embedded in an organic matrix". In: *The journal of physical chemistry letters* 6.3 (2015), pp. 446–450.

[58] Pil J Yoo et al. "Polymer elasticity-driven wrinkling and coarsening in high temperature buckling of metal-capped polymer thin films". In: *Physical review letters* 93.3 (2004), p. 034301.

Chapter 4

Dielectrophoretic assembly of quantum dots into PDMS microlenses

4.1 Introduction

Lithium Niobate

Lithium niobate (LN) is a ferroelectric human made crystal, non existing in nature, of general formula $LiNbO_3$ characterized by large birefringent, pyroelectric, piezoelectric, electro-optic, elastic, photoelastic, and bulk photovoltaic effects. The great amount of physical properties have made LN crystals adopted in a large variety of applications in acoustic, optics, photoelectronic, memory devices, holograms, and others. [1, 2, 3, 4]

The Curie temperature for LN is approximately 1210°C Above this temperature the crystal is paraelectric and non-polar consisting of planar sheets of oxygen atoms in an hexagonal close-packed configuration. The octahedral interstices are equally filled, one-third each, by lithium atoms, niobate atoms and one-third vacant. The sequence, going in the +c direction, is: Li, Nb, vacancy. [5, 6] Figure 4.1 shows the conventional hexagonal unit cell for LiNbOa. Below the Curie temperature the elastic forces become stronger and the lithium and niobate ions are forced in different positions. Those two atoms are not anymore centered between oxygen layers resulting in a spontaneous polarization. For this reason the LN belongs to the displacement

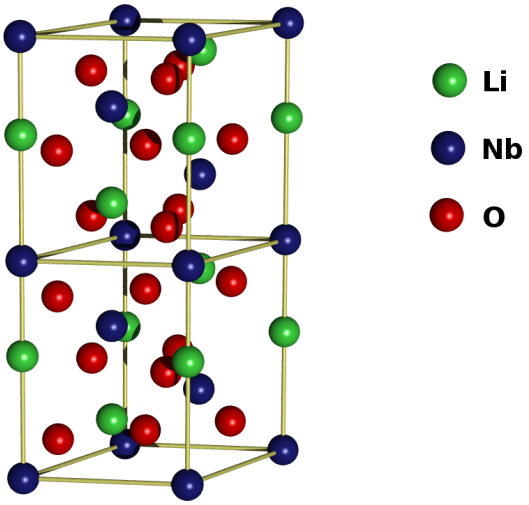

Figure 4.1: Crystal structure of lithium niobate. (Created by Ahellwig with Povray 3.6, CC BY-SA 3.0, https://commons.wikimedia.org/w/index.php?curid=163749)

ferroelectrics class. [7] In order to determine the direction of the c axis two methods are commonly used:

- upon compression of the crystal in c direction the positive direction is coming out from the face that becomes electrically negative[8]
- upon cooling the +c direction comes out of the positive face[9]

In the first case the compression brings the ions move closer to the oxygen layer leaving an excess of negative charge on the +c face; in the second case the temperature contraction pulls the ions further from the oxygen layer producing the excess of surface positive charge.

LN is a very strong pyroelectric material and changes its spontaneous polarization when it is subjected to a temperature variation. The linear relation that bonds the spontaneous polarization $\Delta\mathbf{P}$ and the change in temperature ΔT can be written as:

$$\Delta\mathbf{P} = p\Delta T \tag{4.1}$$

where p is pyroelectric tensor that, since the ions move only in the c direction,

can be expressed as:

$$p = \begin{bmatrix} 0 \\ 0 \\ p_3 \end{bmatrix} \tag{4.2}$$

where p_3 is the only component different from zero of the matrix and its value is $p_3 = -4 \times 10^{-5}$ C/K^{2}m and the sign minus is related to the positive charging of the +c face upon cooling.[10]

Because of the ferroelectricity LN can be locally or periodically poled usually using an electric field poling (EFP) process where a sufficiently intense external electric field is applied in order to exceed the coercive field of the material. In this way crystalline structure of the material can be locally inverted obtaining structures with domain patterns usually in the range going from tens of μm to hundreds of nm [11]

Dielectrophoresis

Electrokinetic forces have been extensively used to manipulate and isolate particles in suspension or to structure liquids overcoming surface tensions using sufficiently strong electric field.[12] The dielectrophoresis permit the manipulation of biological, organic and inorganic particles down to sub-micron dimension.[13, 14] The motion of particle is the balance between gravitation, dielectrophoretic, Bronian and drag forces. Moreover the flux of the dispersant fluid caused by the electrohydrodynamic forces should also be taken into account. For these reason all these forces are quantitatively analysed in the following paragraphs based on the work of Castellanos *et Al* [15].

Stokes force: Consider a spherical particle of mass m and radius a, in a fluid with viscosity μ, and subjected to a force $\mathbf{F}$, its motion is governed by

$$m\frac{d\mathbf{u}}{dt} = -\gamma(\mathbf{u} - \mathbf{v}) + \mathbf{F} \tag{4.3}$$

where $\mathbf{u}$ is the particle velocity, v the fluid velocity and $-\gamma(\mathbf{u} - v)$ is the drag force. The factor γ is the friction factor of the particle that for a spherical particle is equal to $\gamma = 6\pi\eta a$. As the acceleration of sub micron

particles is fast compared to characteristic time of observation ($\tau_a = m/\gamma \rightarrow \tau_a = (\frac{2}{9})(\rho p a^2/\eta)$), we can assume that they always move at their terminal velocity, and that the velocity of the particles is the sum of the fluid velocity plus the motion induced by the external force

$$\mathbf{u} = \mathbf{v} + \frac{\mathbf{F}}{\gamma} \tag{4.4}$$

Gravity: The influence of gravity on particles of density ρ_p suspended in a fluid of density ρ_m is given by

$$\mathbf{F}_g = v(\rho_p - \rho_m)\mathbf{g} \tag{4.5}$$

where g is the gravitational acceleration and v the volume of the particle, so the velocity of a spherical particle in a gravitational field is

$$\mathbf{u}_g = \frac{v|\rho_p - \rho_m|\mathbf{g}}{f} = \frac{2}{9}\frac{a^2|\rho_p - \rho_m|\mathbf{g}}{\eta} \tag{4.6}$$

Dielectrophoresis: The interaction between a non-uniform electric field and a dielectric particle generates the dielectrophoretic force. The electric field phasor induces a dipole phasor in the particle given by $\mathbf{p}(\omega) = v\alpha(\omega)\mathbf{E}$, where α is the effective polarizability of the particle and ω is the angular frequency of the electric field. The time-averaged force acting on the particle is given by

$$\langle \mathbf{F}_{\mathrm{DEP}} \rangle = \frac{1}{2}\mathcal{R}[(\mathbf{p}\cdot\nabla)\mathbf{E}^* = \frac{1}{4}v\mathcal{R}[\alpha]\nabla|\mathbf{E}|^2 - \frac{1}{2}v\mathcal{I}[\alpha](\nabla \times (\mathcal{R}[\mathbf{E} \times \mathcal{I}[\mathbf{E}]) \tag{4.7}$$

where $*$ indicates complex conjugation, $\mathcal{R}[A]$ and $\mathcal{I}[A]$ the real and imaginary parts of A and $|\mathbf{E}|^2 = \mathbf{E}\cdot\mathbf{E}^*$ that lead to a DEP-velocity for a spherical particle equal to

$$\mathbf{u}_{\mathrm{DEP}} = \frac{v\mathcal{R}[\alpha]}{4\gamma}\nabla|\mathbf{E}|^2 = \frac{a^2\varepsilon}{6\eta}\mathcal{R}\left[\frac{\tilde{\varepsilon}_p - \tilde{\varepsilon}}{\tilde{\varepsilon}_p + 2\tilde{\varepsilon}}\right]\nabla|\mathbf{E}|^2 \tag{4.8}$$

In this equation $\tilde{\varepsilon}$ is the complex permittivity defined as $\tilde{\varepsilon} = \varepsilon - i\sigma/\omega$, ε and σ are respectively the permittivity and the conductivity. A very important role is played by the expression in bracket also called the Clausius-Mossotti (CM) factor. The direction of the DEP force depends on the sign of the CM factor, that can vary between $+1$ and $-\frac{1}{2}$ so it can be either attractive or repulsive.

Brownian motion: The Brownian motion is a very important phenomenon when analysing the behaviour of colloidal particles. It is characterized by a zero time average (for t sufficiently long) and is strongly influenced by the temperature of the system. The Gaussian profile of the displacement has a root-mean-square given by

$$\Delta x = \sqrt{2Dt} = \sqrt{\frac{k_B T}{3\pi a \eta} t} \tag{4.9}$$

where k_B is Boltzman's constant, T is the absolute temperature and t is the period of observation. If the motion externally induced by the DEP force is smaller than the random Brownian motion the movement cannot be precisely controlled in period of time shorter than t. For a collection of particles the average movement of the assemble can be considered and the Brownian motion are negligible.

Electrohydrodynamic

Electromagnetic equations Maxwell's equations describe the electromagnetic field in the bulk of materials. The energy is stored both in the magnetic and in the electric fields. Under the assumption that the first is negligible with respect to second, that we can express with the condition

$$\frac{W_M}{W_E} = \frac{(1/2)\mu H^2}{(1/2)\varepsilon E^2} \ll 1 \tag{4.10}$$

where μ and ε are the magnetic and dielectric permeability of the medium, Maxwell's equations can be reduced to the quasi-electrostatic form:

$$\nabla \cdot (\varepsilon \mathbf{E}) = \rho_q \tag{4.11}$$

$$\nabla \times \mathbf{E} = 0 \tag{4.12}$$

$$\nabla \cdot \mathbf{j} + \frac{\partial \rho_q}{\partial t} = 0 \tag{4.13}$$

where ρq is the volume charge density. In the bulk electrolyte, the electric current $\mathbf{j}$ is given by Ohm's law, $\mathbf{j} = \sigma \mathbf{E}$. A very important factor is the electrical Reynolds number [16] defined as the combination of parameters $\varepsilon v / l\sigma$. It can be demonstrated that, since the electrical Reynolds number is very low for common systems, the electrical and the mechanical responses are usually decoupled. Now we can combine Equations 4.11 and 4.13 obtaining that for the complex vector $\mathbf{E}$ it has to be

$$\nabla \cdot ((\sigma + i\omega\varepsilon)\mathbf{E}) = 0 \tag{4.14}$$

where is now a complex vector. The electric field can be decomposed, in many cases where the gradient in permittivities and conductivities are small, into to terms as following

$$\mathbf{E} = \mathbf{E}_0 + \mathbf{E}_1 \quad \text{with} \quad |\mathbf{E}_1| \ll |\mathbf{E}_0| \tag{4.15}$$

and the following equations are satisfied

$$\nabla \cdot \mathbf{E}_0 = 0 \tag{4.16}$$

$$\nabla \cdot \mathbf{E}_1 + \left(\frac{\nabla\sigma + i\omega\nabla\varepsilon}{\sigma + i\omega\varepsilon} \right) \cdot \mathbf{E}_0 = 0 \tag{4.17}$$

Therefore the charge densities can be approximated to

$$\rho_0 = \varepsilon \nabla \cdot \mathbf{E}_0 = 0 \tag{4.18}$$

$$\rho_1 = \varepsilon \nabla \cdot \mathbf{E}_1 + \nabla \varepsilon \cdot \mathbf{E}_0 = \left(\frac{\sigma \nabla \varepsilon - \varepsilon \nabla \sigma}{\sigma + i\omega\varepsilon} \right) \cot \mathbf{E}_0 \tag{4.19}$$

Mechanical equations In order to determine the effect of the electrohydrodynamic field on a fluid the Navier–Stokes equations, for incompressible liquids, should be taken into account:

$$\nabla \cdot \mathbf{v} = 0 \tag{4.20}$$

$$\rho_m \left(\frac{\partial \mathbf{v}}{\partial t} + (\mathbf{v} \cdot \nabla)\mathbf{v} \right) = -\nabla p + \eta \nabla^2 \mathbf{v} + \mathbf{f}_E + \rho_m \mathbf{g} \tag{4.21}$$

where $\mathbf{f}_E$ and $\rho m \mathbf{g}$ are the electrical and gravitational forces. For micrometric system the (usual) Reynolds number is very small so the convective term can be neglected. If we combine this assumption with the time average of the external electrical force we obtain the following expression for the average fluid velocity

$$0 = -\nabla p + \eta \nabla^2 \mathbf{b} + \langle \mathbf{f}_E \rangle + \Delta \rho_m \mathbf{g} \tag{4.22}$$

where can be demonstrated that $\langle \mathbf{f}_E \rangle$ is equal to

$$\langle \mathbf{f}_E \rangle = \frac{1}{2} \mathcal{R}(\rho_q \mathbf{E}^*) - \frac{1}{4} \mathbf{E} \cdot \mathbf{E}^* \nabla \varepsilon \tag{4.23}$$

Now we can substitute in the previous equation the two expression derived for the charge density from Equations 4.18 and 4.19:

$$\langle \mathbf{f}_E \rangle = \frac{1}{2} \mathcal{R} \left(\left(\left(\frac{\sigma \nabla \varepsilon \varepsilon \nabla \sigma}{\sigma + i\omega\varepsilon} \right) \cdot \mathbf{E}_0 \right) \mathbf{E}_0^* \right) - \frac{1}{4} \mathbf{E}_0 \cdot \mathbf{E}_0^* \nabla \varepsilon \tag{4.24}$$

The combination of Equations 4.22 and 4.24 describes the electrohydrodynamic forces acting on a incompressible fluid under the action of an external electric field.

4.2 Article

4.2.1 Authors and affiliations

- Sara Coppola[a]
- Giuseppe Nasti[b,c]
- Biagio Mandracchia[a,b]
- Veronica Vespini[a]
- Simonetta Grilli[a]
- Vito Pagliarulo[a]
- Paola Pareo[d,e]
- Michele Manca[d]
- Luigi Carbone[f]
- Giuseppe Gigli[f]
- Pietro Ferraro[a]

[a] Applied Sciences and Intelligent Systems, Consiglio Nazionale delle Ricerche, Pozzuoli 80078, Italy.

[b] Department of Chemical Materials and Production Engineering, University of Naples Federico II, Napoli 80138, Italy.

[c] Institute for Polymers Composites and Biomaterials, Consiglio Nazionale delle Ricerche, Pozzuoli 80078, Italy.

[d] Center for Biomolecular Nanotechnologies, Fondazione Istituto Italiano di Tecnologia, Arnesano 73010, Italy.

[e] Department of Innovation Engineering, University of Salento, Lecce 73100, Italy.

[f] National Nanotechnology Laboratory, Nanoscience Institute of Consiglio Nazionale delle Ricerche, Arnesano 16-73100, Italy.

4.2.2 Introduction

Self-assembling processes are very powerful approaches that are gaining even more credit in chemistry and materials industry for micro- and nanoscale technology due to their intrinsic advantages of simplicity, versatility and rapidity.[17, 18, 19] Polymers in liquid phase appear as very suitable candidates to be processed by direct self-assembling methods thus avoiding lithography or long-lasting moulding multi-steps processes.[20, 21, 22, 23, 24, 25] In fact, the self-assembling strategy could allow the fabrication of components and devices in a single step working directly onto polymer solutions. Nowadays, polymers are multipurpose materials that are ubiquitous in all modern micro and biotechnologies. For instance, polymer three-dimensional (3-D) microstructures have become very promising components in optics, electronic, photonics and biomaterials fields. Microlens arrays, which generally refer to 2-D arrays of small lenses with diameters in the range of ten to hundreds of micrometers, represent important types of miniaturized optical components used in a wide range of applications. [26, 27, 28, 29] In particular, microlenses from polymer solutions [30, 31] could offer interesting advantages like easy fabrication approach and the use of sustainable/user-friendly materials. High definition displays, photovoltaic devices, semiconductor solar cells, light emitting diodes [32, 33], sensor [34], biochemical assays [30] and artificial compounds eyes [35] offer just an example of the considerable extension of interest for the micro-technologies industries. Only very recently polymer-based nanocomposite materials have attracted considerable interest because of their excellent properties compared to polymeric materials. [36, 37] In fact, the incorporation of nanofillers into the polymer matrix could modulate the resulting properties of the nanocomposite produced and, at the same time, allows one to use the existing fabrication methods. The growing interest in arrays of polymer microstructures is due to the fact that it is relatively easy for polymers to incorporate colloidal inorganic nanocrystals (NCs) or quantum dots (QDs), thus transforming originally passive micro-optical elements into active photonic components by combining the processability of organic materials with efficient luminescence displayed by the nanofillers.[38]

This has been proved to be of great interest for novel applications such as the fabrication of photonic crystals [39] and, notably, of innovative solar cells showing enhanced efficiency. [40, 41, 42] Here we demonstrate an innovative formation process based on pyro-electrohydrodynamics (pyro-EHD) for direct formation of self- assembled polymer microstructures. Colloidal inorganic NCs embedded into a polymer matrix are dispensed onto a ferroelectric substrate and self-assembled in a single step. Essentially a simultaneous two-fold self-assembling process, involving either EHD instability acting on the hosting liquid polymer in conjunction with dielectrophoretic (DEP) forces operating on NCs, allows the realization of an active array of microstructures just in a single step. Pyro- EHD and pyro-DEP have been discovered and applied separately as advanced processes for the self-assembling of nanofillers [43, 44, 45], liquids and polymers, including Polydimethylsiloxane (PDMS) [46, 47, 48, 49, 50] in a multiscale range (i.e., between 25 to 200 μm diameter) with high degree of uniformity. By controlling the polymer instability driven by EHD, different micro-optical structures can be obtained spontaneously, i.e., spherical or toroidal.[51] Here we show how the thermal stimulus applied to a periodically poled lithium niobate crystal (PPLN) is able to drive in a single step the self-assembling and subsequently the cross-linking of the liquid PDMS matrix in form of a 2-D micro-optical polymer array. Meanwhile the liquid polymer is shaped by the EHD instability into a micro-structures array, the NCs are collected through DEP forces at bottom of each optical element of the layer. We show that the formed nanocomposite layer behave indeed as effective active optical elements so that the process does not change the NCs properties. The fabrication procedures of NCs-incorporated and light-converting is illustrated and described. Full optical characterization is also performed and reported. Such self-assembling of nanocomposite polymer could inspire future fabrication techniques for producing layers that could be mounted on top of OLED devices in order to drive the light in a more efficient way, for improving photovoltaic efficiency in energy applications or even for detecting and imaging fluorescent objects in bio-technology.

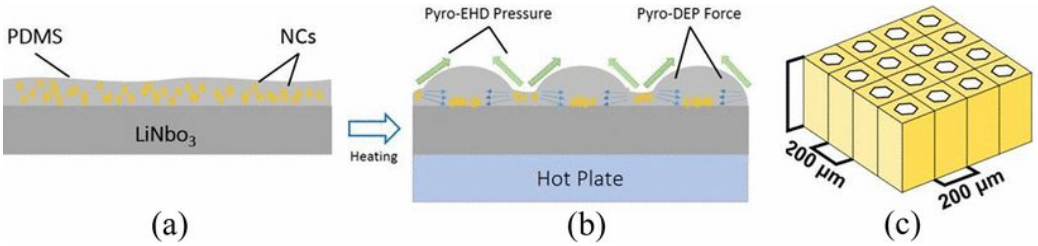

Figure 4.2: Microlenses arrays self-assembling is triggered by heating the Lithium Niobate: (a) A polymer film with NCs embedded is spin coated onto the upper surface of the PPLN. (b) The fabrication procedure induces both PDMS microlenses formation by Pyro-EHD pressure and NCs positioning by Pyro-DEP force. (c) PPLN hexagonal geometry array of Lithium Niobate inverted domain.

4.2.3 Fabrication process

Figure 4.2(a) and (b) shows the schematic view of the self-assembling process. The colloidal inorganic CdSe/CdS core/shell quantum nanorods [52] were incorporated into a matrix of PDMS (Dow Corning Sylgard 184, 10:1 mixing ratio, base to curing agent Midland; Formula cP, Formula from datasheet) through the use of toluene as common blending solvent.

PDMS was firstly dissolved in toluene (8 wt%) by ultrasonication for 1 h and vigorously shaken overnight thereafter. Afterwards, different volumes of TOP-capped CdSe/CdS NRs (10^{-8} M in toluene) were added to PDMS solutions to obtain nanocomposite blends with different relative NRs/PDMS concentrations ∼0.1 wt%. A PPLN crystal with a 200 µm squared lattice of hexagonal domains was adopted to drive the process (see Figure 4.2(c)). The PPLN substrate was fabricated by the reversion of the uniform spontaneous polarization of commercially available congruent z-cut LN crystals by electric field poling. The period resist pattern (Micro resist technology ma-P1210) was generated by standard photolithography and is required to ensure the inversion selectivity of the ferroelectric domains. [53] The electric field poling process consists in a positive voltage pulse, lasting about 400 ms, slightly exceeding the coercive field of LN (<21 $kVm^{-1}m$), applied on the patterned crystal face by using a liquid electrolyte (i.e., LiCl in deionized water) at a room temperature. The liquid electrode configuration has two chambers

which squeeze the sample between two O-ring rubber seals.

The resulting sample used in the experiments consists of a square array of bulk reversed domains with a period ∼200 μm along both x- and y-directions. The sign of the pyroelectric coefficient is reversed according to the inverted ferroelectric domains.

After standard solvent cleaning (the sample was submerged in Acetone ultrasonic cleaner for 5 min and then washed with ethanol) the PPLN crystal was spin coated with 10 μL of the NCs mixture for 60 s and successively heated at 170 °C for 30 s onto a conventional hotplate. The thermal stimulus induced simultaneously the formation of PDMS microstructures array, the DEP distribution of the NCs and the curing of the polymer. The fabrication process of multiscale PDMS array based on the EHD self-assembling method, was demonstrated as a straight-forward, fast and simple process suitable to achieve structures with lens/donuts shapes having several size.[51] The geometrical and the optical characteristics of the passive polymer microlenses have been also demonstrated. The experiments reported in the following describe the self-assembling of NCs into the active polymer layer. Figure 4.3(a) shows the polymer self-assembling in correspondence of four hexagonal regions. The image acquired in bright filed displays the accumulation of PDMS into four circular regions in correspondence of the hexagon profile. Figure 4.3(b) represents the same field of view acquired in fluorescence mode making visible and clear the NCs distribution.

The NCs are patterned in two distinctly concentric regions, the core of the hexagon and the outer limiter of the polymer lens, conveyed by the self- assembling process along the region of high pyro-electric field. As a consequence of the pyro-DEP force, they are attracted to the center on the back surface region of the hexagons, as clearly visible in the confocal image of the horizontal side of Figure 4.3(c).

The spin speed allows one to tune the geometry of the microstructures shaping the active polymer layer.[51] We identified the better condition in term of the rounds per minute (RPM) for shaping the micro-elements at 4000 RPM. The microscope observation in Figure 4.4 was performed recording the final frame at the end of the heating procedure in bright filed (top) or in

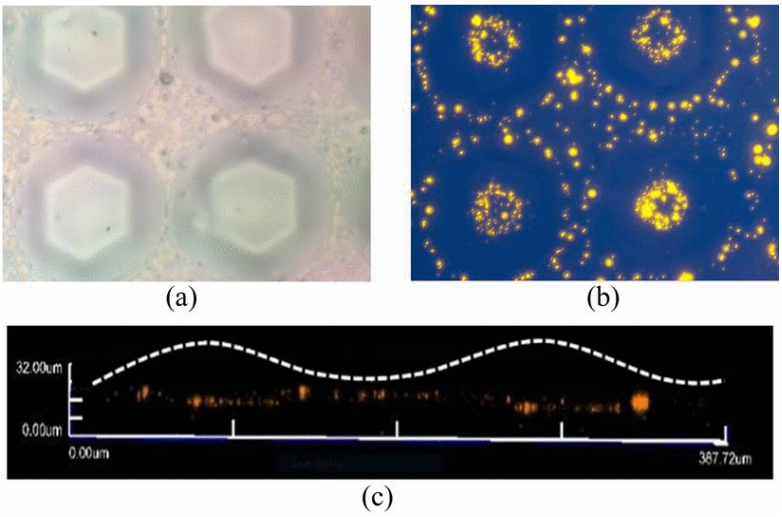

Figure 4.3: Bright field (a) and fluorescence image emission of nanorods (b) in correspondence of four hexagonal regions. (c) Confocal image of the horizontal side view in the xz plane of two adjacent hexagons, the NCs are attracted in the central region of the hexagon as a consequence of the pyro-DEP force.

fluorescence condition (bottom). The profile of the micro-optical elements revealed by the stylus profiler measurements (DektakXT, Bruker) show an height of about 7 μm at spinning rate of 4000 RPM.

Increasing the spin speed, the micro-optical elements appear to be distant one from the other with a quite low height while the inter-gap space of two adjacent microstructures increases.[51] In the bottom image of Figure 4.4 the fluorescence microscope pictures clearly reveal the NCs self-collection inside the hexagons of the PPLN substrate. The results show that the presence of NCs does not affect the global behavior of the liquid polymer under the action of the pyro-EHD pressure, so that the physics remains the same as described in the previous papers. [51, 54, 55] The LN is a ferroelectric solid crystal and exhibits a change in electric polarization as a function of temperature because of its pyroelectric properties. In fact, this crystal shows pyroelectricity at room temperature and this phenomenon is related to the relative movement of lithium and niobium ions through oxygen layers in the crystal lattice.[49] The relation between the electric polarization vector, P,

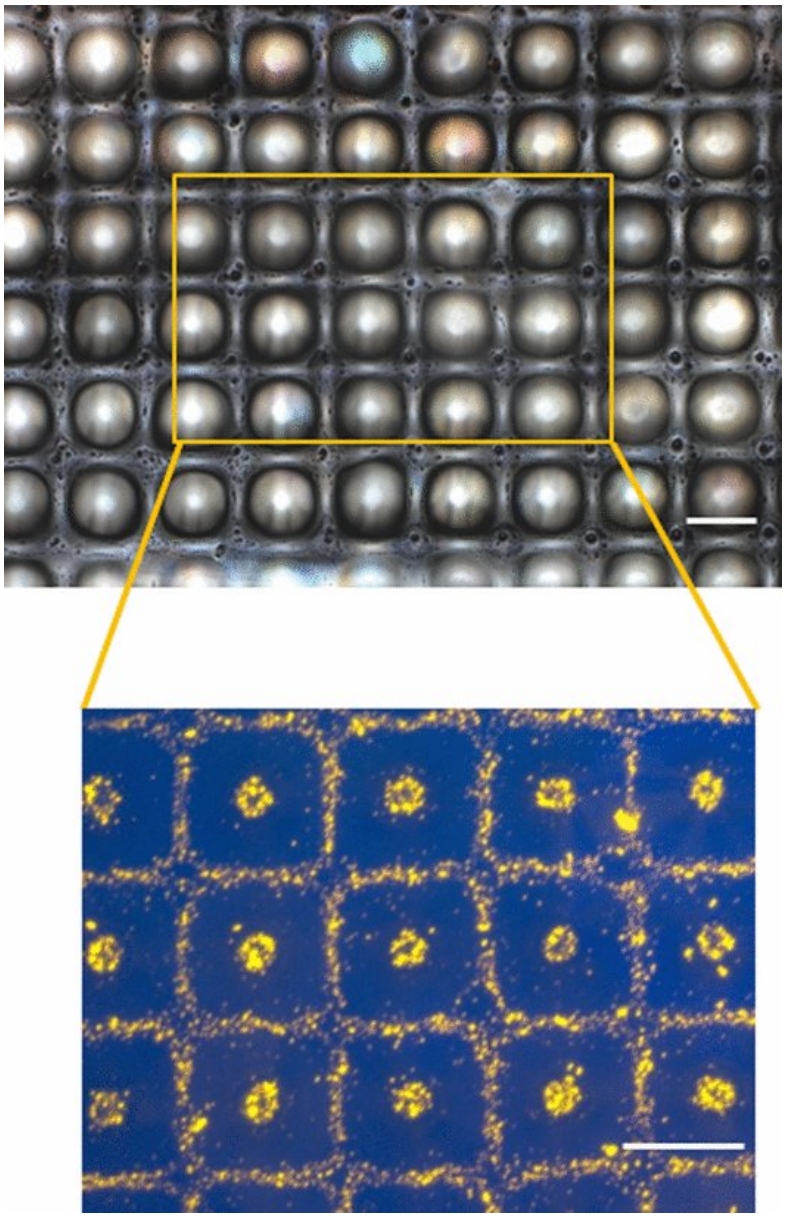

Figure 4.4: Bright filed image (top) compared to that acquired in fluorescence modality (bottom) evidencing the self-collecting of nanorods in the center and on the border of the hexagonal cell (scale bar 100 μm).

and the temperature variation, ΔT, can be written as $P = P_0 + p(T - T_0)$, where P_0 is the equilibrium polarization at the temperature T_0 and p is the pyroelectric vector defined as $p_i = \partial P_i / \partial T$. As this movement only happens in the c-axis direction the only non-zero component of the pyroelectric tensor for LN is $p = -4 \times 10^{-5}$ C K^{-1} m^{-2} where the negative sign indicates that the +c crystal face becomes more negative for a positive variation of the temperature.[10] It is well known that at the equilibrium, all Ps in the crystal are fully screened by the external screening charge and no electric field exists.[11] The change of the polarization, occurring with the temperature variation, perturbs such equilibrium, causing a lack or excess of surface screening charges.[56] Consequently, an electrostatic state appears and generates a high electric field at the crystal surface. Electrical neutral particles dispersed in a fluid medium, such as the NCs into the PDMS matrix, exhibit a dipole moment when subjected to the pyroelectric field. In particular, the dipole moment and the electric field are parallel or antiparallel if the particles are more or less polarizable than the medium, respectively. Overall, both the edges of polarized particles are subjected to a force directed to the opposite charged electrode. If the electric field is spatially uniform, these forces are equal in modulus and opposed in direction so no net force acts on the particle. In case of a spatially non-uniform field the resultant is non-zero and the particles are attracted or rejected towards the region of strongest field intensity. This effect is called DEP [57] and the DEP force acting on a particle subjected to a stationary electric field E is expressed in Equation (4.25):

$$F = 4\pi r^3 \Re\left[K\right] E \cdot \nabla E = 2\pi r^3 \Re[K] \cdot \nabla E^2 \tag{4.25}$$

where r is the radius of the particle, K is the Clausius–Mossotti factor. The DEP force direction is independent of the polarity of the electric field gradient and can be either attractive or repulsive. If the particle conductivity is higher than the medium conductivity the Clausius–Mossotti factor is positive and the force is directed toward the regions of higher intensity of the electric field (positive DEP), otherwise they are driven toward regions of lower intensity (negative DEP). We used the COMSOL finite element method software

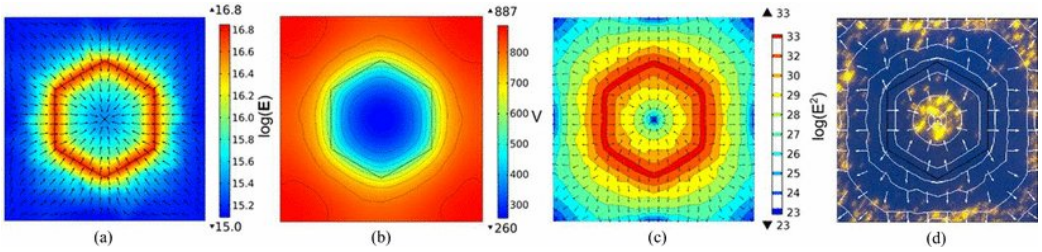

Figure 4.5: Numerical simulation of electric field (a), electric potential (b) and DEP force (c) on top surface of LN generated pyroelectrically ($\Delta T = 100$ [K]). (d) Superposition of the DEP-force intensity contour lines onto a fluorescence image of a singular region, the white arrows indicate the areas of attraction due to high values of the pyro-electric field.

package for simulating the forces generated onto the crystal. The pyroelectric effect was implemented by the Remanent electric displacement constitutive relation by using the following electric current module in stationary condition:

$$D = \varepsilon_0 \varepsilon_r \cdot E + D_r = \varepsilon_0 \varepsilon_r \cdot E + p \nabla T \tag{4.26}$$

where D is the electric displacement field, p is the dipole momentum vector, T the temperature applied, ε_0 is vacuum dielectric constant, ε_r is relative permittivity matrix. Figure 4.5 (a) shows the logarithm of electric field modulus and the electric field vectors. It is worth noting that the maxima of the electric field distribution are located on the edges of the hexagonal inverted domain and that all the vectors point to the center of the cell. Figure 4.5(b) shows the electric potential on the surface of the LN crystal generated by a temperature variation of 100 K. The DEP force vectors and the electric field contour lines for the case of negative Clausius–Mossotti factor ($R[K] < 0$) are presented in Figure 4.5(c). The effect of this force field is to push the NCs away from hexagonal edges and to crowd them into the centre and on the border of the cell. This is in excellent agreement with the experimental evidence as shown in Figure 4.5(d) where the superposition of Formula contour lines and the fluorescence image of the particles is reported.

The optical properties of the active nano-composite layer were also accurately characterized through an interferometry technique. The sample is

put into the object arm of a Mach–Zehnder interferometer, provided with a continuous laser source emitting at a wavelength of 532 nm. By appropriate numerical manipulation of the interferograms recorded by the CCD it is possible to obtain the wavefront curvature transmitted by the sample at a given distance. We report the interferometric analysis on a single microlens fabricated at 6000 rpm. Microlens surface profile and geometrical properties have been reconstructed by transmission plane-wave test. The lens surface profile was reconstructed from the wavefront curvature at the image plane, the interferometric technique used was based on digital holography in microscope configuration set-up. [58, 59] We have recovered the geometrical parameters by fitting the wavefront curvature as depicted in Figure 4.6, where the focal length is calculated from the radius of curvature of the wavefront. It is important to note that the shape of the lens is not perfectly spherical. In fact, the shape deviates from a sphere having a slight concave surface at the center. We believe this very little concave profile is due to the starting thickness of the polymer layer and to the kinetic behavior of slowly solvent evaporation process in the droplet, well known in the literature.[60] The shape of the passive PDMS microlens arrays produced by EHD assembly in a multiscale range (i.e., between 25 to 200 μm diameter) with high degree of uniformity has been deeply investigated [35]. The same results are confirmed in case of microlenes with an underlying NCs active layer. Nevertheless the lens shape does not appear to be essential for improving the brightness and electroluminescence efficiency of the micro-devices. In fact, we could insert an appropriate diffusor and evaluate the total emission of the full lensed polymer array, so that the parallel emission of multiple lenses could be used to overcome some losses eventually related to the geometrical parameters.

When it comes to describe the embedded NCs fluorescence behavior, theoretical optical parameters are not totally reliable. For this reason we have experimentally measured parameters such as NCs fluorescence focal length and depth of focus by scanning the emerging light field along the optical axis. Measurements were performed using a Zeiss Axio Imager M1 microscope in epi- fluorescence mode. In this mode the NCs layer underlying the micro optical array is excited by the light coming from the microscope illumina-

Figure 4.6: Phase maps (left) of single microlens made at 6000 RPM. The dashed lines correspond to reconstructed microlens profile shown on the right.

tor. At same time NCs fluorescence emission is collected by a 10× objective. Three-dimensional intensity maps were obtained moving the objective by 5 µm steps above the sample plane so that images were recorded at different heights in a z-ascending order using an AxioCam CCD camera.

Figure 4.7 depicted the principle of light conversion through the lensed array in z- axis. In order to demonstrate the electroluminescence emission of the micro- optical elements we reported the measure regarding the characterization of the real spot of emission. In fact, the fluorescence spots of the 3×4 microlenses array reported in Figure 4.7(a) were recorded through the z-stack analysis at a focal distance of 85 mm. The fluorescence focal length was taken as a function of the distance between the sample plane and the point of maximum on-axis fluorescence intensity. The Figure 4.7(b) was constructed to better explain the fluorescence emission: the microlens is excited by the light coming from the microscope and focused through a 10× objective, the green emission reported is the real measure of the NCs fluorescence intensity behaviour evidencing in yellow the focal spots. Averaging the values recorded for a sample of 12 microlenses a mean fluorescence focal length 90 mm for the microlens arrays was calculated. The fluorescence depth of focus was considered as the distance where the peak intensity has decreased to 80% of the peak value, as reported in Figure 4.7(c).

Measurements of the fluorescence spectrum showed a 9 nm blue- shift in nanorods emission spectrum from the nominal emission maximum. These measurements were made using a self-built micro-photoluminescence setup:

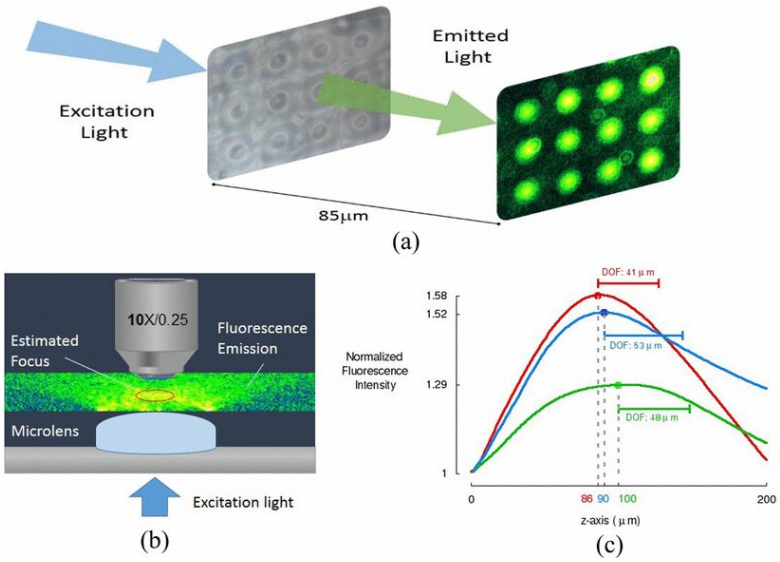

Figure 4.7: Microlenses arrays focus the fluorescence light emitted by NCs: (a) Schematic view of NCs fluorescence acquisition and (b) overview of the micro-photoluminescence setup. (c) Normalized fluorescence intensity along the z-axis.

the main components are a 450 nm laser source, two microscope objectives, a multimode fiber and an Ocean Optics QE65000 Spectrometer. The blue laser light is focused by a 50× objective on a 100 nm-wide spot in order to excite the nanorods under a single micro-lens while the nanorods emission light is collected by a 20× objective and sent to the spectrometer by an 8 mm-wide multimode fiber. Controlling the movement along the z-direction (i.e., axial direction) it was possible to measure the spectrum of light propagating from a 400 nm-wide emitting spot of an individual micro-lens. It is very interesting to note that even if the NCs distribution and self-collection is not very regular, the final spot of fluorescence appears to be uniform.

4.2.4 Conclusions

In summary, a novel direct patterning process for the fabrication and the functionalization of a nanocomposite polymer layer by DEP self-collection has been presented. The challenging aspect is the single-step feature of the process proposed in which the self-assembling of liquid polymer in a micro-

optical array occurs at same time with the collection of the NCs in arrayed sites. To the best of our knowledge this is the first time that a two-fold self-assembling process allows the shaping of liquid in a micro-optical array and simultaneously the collection of NCs in specific locations. Moreover, the process is rapid and, although the uniformity of the dispersion is not yet optimal, the fabrication process can be very promising in case of further improvements in dispersing NCs or QDs into the polymer thus making the microstructures more reliable. However the reported experimental characterizations show that lenses work properly and the final spots of fluorescence produced by lensed array appear to be uniform.

References

[1] Luis Arizmendi. "Photonic applications of lithium niobate crystals". In: *physica status solidi (a)* 201.2 (2004), pp. 253–283.

[2] Ed L Wooten et al. "A review of lithium niobate modulators for fiber-optic communications systems". In: *Selected Topics in Quantum Electronics, IEEE Journal of* 6.1 (2000), pp. 69–82.

[3] K Buse, A Adibi, and D Psaltis. "Non-volatile holographic storage in doubly doped lithium niobate crystals". In: *nature* 393.6686 (1998), pp. 665–668.

[4] MN Armenise. "Fabrication techniques of lithium niobate waveguides". In: *Optoelectronics, IEE Proceedings J.* Vol. 135. 2. IET. 1988, pp. 85–91.

[5] SC Abrahams, HJ Levinstein, and JM Reddy. "Ferroelectric lithium niobate. 5. Polycrystal X-ray diffraction study between 24 and 1200 Celsius". In: *Journal of Physics and Chemistry of Solids* 27.6 (1966), pp. 1019–1026.

[6] Yiping Guo, Kenichi Kakimoto, and Hitoshi Osato. "Phase transitional behavior and piezoelectric properties of". In: *Applied physics letters* 85.18 (2004), pp. 4121–4123.

[7] SC Abrahams, JM Reddy, and JL Bernstein. "Ferroelectric lithium niobate. 3. Single crystal X-ray diffraction study at 24 Celsius". In: *Journal of Physics and Chemistry of Solids* 27.6-7 (1966), pp. 997–1012.

[8] JG Brainerd et al. "Standards on piezoelectric crystals". In: *Proc. IRE* 37 (1949), pp. 1378–1395.

[9] GD Boyd et al. "LiNbO3: an efficient phase matchable nonlinear optical material". In: *Applied physics letters* 5.11 (1964), pp. 234–236.

[10] RS Weis and TK Gaylord. "Lithium niobate: summary of physical properties and crystal structure". In: *Applied Physics A* 37.4 (1985), pp. 191–203.

[11] S Grilli et al. “In situ investigation of periodic poling in congruent LiNbO3 by quantitative interference microscopy”. In: *Measurement Science and Technology* 19.7 (2008), p. 074008.

[12] Pei Yu Chiou, Aaron T Ohta, and Ming C Wu. “Massively parallel manipulation of single cells and microparticles using optical images”. In: *Nature* 436.7049 (2005), pp. 370–372.

[13] Peter RC Gascoyne and Jody Vykoukal. “Particle separation by dielectrophoresis”. In: *Electrophoresis* 23.13 (2002), p. 1973.

[14] Ronald Pethig and Gerard H Markx. “Applications of dielectrophoresis in biotechnology”. In: *Trends in biotechnology* 15.10 (1997), pp. 426–432.

[15] Antonio Castellanos et al. “Electrohydrodynamics and dielectrophoresis in microsystems: scaling laws”. In: *Journal of Physics D: Applied Physics* 36.20 (2003), p. 2584.

[16] JR Melcher and GI Taylor. “Electrohydrodynamics: a review of the role of interfacial shear stresses”. In: *Annual Review of Fluid Mechanics* 1.1 (1969), pp. 111–146.

[17] Junhu Zhang et al. “Colloidal Self-Assembly Meets Nanofabrication: From Two-Dimensional Colloidal Crystals to Nanostructure Arrays”. In: *Advanced Materials* 22.38 (2010), pp. 4249–4269. ISSN: 1521-4095. DOI: 10.1002/adma.201000755. URL: http://dx.doi.org/10.1002/adma.201000755.

[18] Benjamin Hatton et al. “Assembly of large-area, highly ordered, crack-free inverse opal films”. In: *Proceedings of the National Academy of Sciences* 107.23 (2010), pp. 10354–10359.

[19] P. Zhu et al. “FDTD Analysis on Extraction Efficiency of GaN Light-Emitting Diodes With Microsphere Arrays”. In: *Journal of Display Technology* 9.5 (2013), pp. 317–323.

[20] Yik-Khoon Ee et al. “Light extraction efficiency enhancement of InGaN quantum wells light-emitting diodes with polydimethylsiloxane concave microstructures”. In: *Opt. Express* 17.16 (Aug. 2009), pp. 13747–13757.

[21] Vinna Lin et al. “An Optical Wavefront Sensor Based on a Double Layer Microlens Array”. In: *Sensors* 11.11 (2011), p. 10293.

[22] Xing Zhao et al. “Microlens-array-enabled on-chip optical trapping and sorting”. In: *Applied optics* 50.3 (2011), pp. 318–322.

[23] Takeyuki Mogi et al. “Real-time detection of DNA hybridization on microarray using a CCD-based imaging system equipped with a rotated microlens array disk”. In: *Biosensors and Bioelectronics* 26.5 (2011), pp. 1942–1946.

[24] Young Min Song et al. “Digital cameras with designs inspired by the arthropod eye”. In: *Nature* 497.7447 (2013), pp. 95–99.

[25] Michael T Gale et al. “Fabrication of continuous-relief micro-optical elements by direct laser writing in photoresists”. In: *Optical Engineering* 33.11 (1994), pp. 3556–3566.

[26] Hongkai Wu, Teri W Odom, and George M Whitesides. “Reduction photolithography using microlens arrays: applications in gray scale photolithography”. In: *Analytical chemistry* 74.14 (2002), pp. 3267–3273.

[27] R Stevens and T Miyashita. “Review of standards for microlenses and microlens arrays”. In: *The Imaging Science Journal* 58.4 (2010), pp. 202–212.

[28] Sadao Hayashi et al. “Imaging by polystyrene latex particles”. In: *Journal of colloid and interface science* 144.2 (1991), pp. 538–547.

[29] Pisist Kumnorkaew et al. “Investigation of the deposition of microsphere monolayers for fabrication of microlens arrays”. In: *Langmuir* 24.21 (2008), pp. 12150–12157.

[30] Yu Lu, Yadong Yin, and Younan Xia. “A Self-Assembly Approach to the Fabrication of Patterned, Two-Dimensional Arrays of Microlenses of Organic Polymers”. In: *Advanced Materials* 13.1 (2001), pp. 34–37.

[31] Tetsuo Tsutsui et al. “Doubling Coupling-Out Efficiency in Organic Light-Emitting Devices Using a Thin Silica Aerogel Layer”. In: *Advanced Materials* 13.15 (2001), pp. 1149–1152.

[32] Yiru Sun and Stephen R Forrest. “Enhanced light out-coupling of organic light-emitting devices using embedded low-index grids”. In: *Nature Photonics* 2.8 (2008), pp. 483–487.

[33] Kiwon Oh et al. “Facile preparation of epoxy nanocomposites with highly dispersed graphite nanosheets and their dielectric properties”. In: *Macromolecular Research* 20.11 (2012), pp. 1197–1200.

[34] Sumanta Sahoo et al. “Modified graphene/polyaniline nanocomposites for supercapacitor application”. In: *Macromolecular Research* 20.4 (2012), pp. 415–421.

[35] MC Schlamp, Xiaogang Peng, and AP Alivisatos. "Improved efficiencies in light emitting diodes made with CdSe (CdS) core/shell type nanocrystals and a semiconducting polymer". In: *Journal of Applied Physics* 82.11 (1997), pp. 5837–5842.

[36] Dan-Chen Cheng et al. "Improving Si solar cell performance using Mn: ZnSe quantum dot-doped PLMA thin film". In: *Nanoscale research letters* 8.1 (2013), pp. 1–5.

[37] Jiafang Li et al. "Fabrication of three-dimensional woodpile photonic crystals in a PbSe quantum dot composite material". In: *Optics express* 14.22 (2006), pp. 10740–10745.

[38] T Trupke, MA Green, and P Würfel. "Improving solar cell efficiencies by down-conversion of high-energy photons". In: *Journal of Applied Physics* 92.3 (2002), pp. 1668–1674.

[39] István Robel et al. "Quantum dot solar cells. Harvesting light energy with CdSe nanocrystals molecularly linked to mesoscopic TiO2 films". In: *Journal of the American Chemical Society* 128.7 (2006), pp. 2385–2393.

[40] Joe Tien, Andreas Terfort, and George M Whitesides. "Microfabrication through electrostatic self-assembly". In: *Langmuir* 13.20 (1997), pp. 5349–5355.

[41] RC Hayward, DA Saville, and IA Aksay. "Electrophoretic assembly of colloidal crystals with optically tunable micropatterns". In: *Nature* 404.6773 (2000), pp. 56–59.

[42] Enoch Kim, Younan Xia, and George M Whitesides. "Two-and three-dimensional crystallization of polymeric microspheres by micromolding in capillaries". In: *Advanced Materials* 8.3 (1996), pp. 245–247.

[43] C Zhang et al. "Dielectrophoretic separation of carbon nanotubes and polystyrene microparticles". In: *Microfluidics and nanofluidics* 7.5 (2009), pp. 633–645.

[44] Pavel Mokry, Milan Marvan, and Jan Fousek. "Patterning of dielectric nanoparticles using dielectrophoretic forces generated by ferroelectric polydomain films". In: *Journal of applied physics* 107.9 (2010), p. 094104.

[45] Eduardo Yraola et al. "Spontaneous Emission and Nonlinear Response Enhancement by Silver Nanoparticles in a Nd3+-Doped Periodically Poled LiNbO3 Laser Crystal". In: *Advanced materials* 25.6 (2013), pp. 910–915.

[46] Xiaolei Xi et al. “The self-assembly and patterning of thin polymer films on pyroelectric substrates driven by electrohydrodynamic instability”. In: *Soft Matter* 8.2 (2012), pp. 298–302.

[47] Lisa Miccio et al. “Hemicylindrical and toroidal liquid microlens formed by pyro-electro-wetting”. In: *Optics letters* 34.7 (2009), pp. 1075–1077.

[48] Simonetta Grilli, Veronica Vespini, and Pietro Ferraro. “Surface-charge lithography for direct PDMS micro-patterning”. In: *Langmuir* 24.23 (2008), pp. 13262–13265.

[49] Francesco Merola et al. “Reversible Fragmentation and Self-Assembling of Nematic Liquid Crystal Droplets on Functionalized Pyroelectric Substrates”. In: *Advanced Functional Materials* 22.15 (2012), pp. 3267–3272.

[50] Veronica Vespini et al. “Pyroelectric Adaptive Nanodispenser (PYRANA) microrobot for liquid delivery on a target”. In: *Lab on a Chip* 11.18 (2011), pp. 3148–3152.

[51] Veronica Vespini et al. “Electrohydrodynamic assembly of multiscale PDMS microlens arrays”. In: *Selected Topics in Quantum Electronics, IEEE Journal of* 21.4 (2015), pp. 399–406.

[52] Luigi Carbone et al. “Synthesis and micrometer-scale assembly of colloidal CdSe/CdS nanorods prepared by a seeded growth approach”. In: *Nano letters* 7.10 (2007), pp. 2942–2950.

[53] G Rosenman et al. “Electron emission from ferroelectrics”. In: *Journal of Applied Physics* 88.11 (2000), pp. 6109–6161.

[54] Pietro Ferraro et al. “Wettability patterning of lithium niobate substrate by modulating pyroelectric effect to form microarray of sessile droplets”. In: *Applied Physics Letters* 92.21 (2008), p. 213107.

[55] Simonetta Grilli and Pietro Ferraro. “Dielectrophoretic trapping of suspended particles by selective pyroelectric effect in lithium niobate crystals”. In: *Applied Physics Letters* 92.23 (2008), p. 232902.

[56] El Mostafa Bourim et al. “Pyroelectric electron emission from- Z face polar surface of lithium niobate monodomain single crystal”. In: *Journal of electroceramics* 17.2-4 (2006), pp. 479–485.

[57] Herbert A Pohl. “The motion and precipitation of suspensoids in divergent electric fields”. In: *Journal of Applied Physics* 22.7 (1951), pp. 869–871.

[58] F Merola et al. “Self-patterning of a polydimethylsiloxane microlens array on functionalized substrates and characterization by digital holography”. In: *Journal of Micromechanics and Microengineering* 19.12 (2009), p. 125006.

[59] IA Grimaldi et al. “Printing of polymer microlenses by a pyroelectrohydrodynamic dispensing approach”. In: *Optics letters* 37.13 (2012), pp. 2460–2462.

[60] Catherine P Whitby, Xun Bian, and Rossen Sedev. “Spontaneous liquid marble formation on packed porous beds”. In: *Soft Matter* 8.44 (2012), pp. 11336–11342.